Porous Cantilever Resonators for Chemical Sensing in Fluid Environments

Steven Noyce

A senior thesis submitted to the faculty of
Brigham Young University
in partial fulfillment of the requirements for the degree of

Bachelor of Science

Robert Davis, Advisor

Department of Physics and Astronomy

Brigham Young University

August 2015

Copyright © 2015 Steven Noyce

All Rights Reserved

ABSTRACT

Porous Cantilever Resonators for Chemical Sensing in Fluid Environments

Steven Noyce
Department of Physics and Astronomy, BYU
Bachelor of Science

Porous cantilever resonator sensors offer detection of trace chemical concentrations in otherwise difficult sensing environments such as gases or liquids. Fabrication of such devices has traditionally been difficult because microfabrication processes that can acheive high aspect ratios are not generally compatible with porous materials. Here we report the fabrication of porous resonators made from a carbon infiltrated carbon nanotube structure. Resulting structure densities are tunable in the range of 10^2 to 10^3 kg/m^3. We perform resonance measurements on these structures in vacuum, air, and water. We also present initial use of these devices as sensors.

Keywords: Cantilever, Sensor, Porous, Chemical, Quality Factor

ACKNOWLEDGMENTS

I gratiously thank Dr. Robert Davis for his mentorship and advisement. I also thank Drs. Richard Vanfleet, David Alred, and Harold Craighead for their time, input, and provision of equipment.

Contents

Table of Contents iv

List of Figures vii

1 Introduction **1**
1.1 Cantilevers as Chemical Sensors . . . 1
1.2 Successes of Current Devices . . . 2
1.3 Limitations of Current Devices . . . 3
1.4 Advantages of Porous Cantilevers . . . 3
1.5 Potential Disadvantages of Porous Cantielvers . . . 4
1.6 Previous Work on Porous Sensors . . . 4
1.7 Limitations in Current Microfabrication Processes . . . 4
1.8 Review of the CNT-M Process . . . 5
1.9 Advantages of the CNT-M Process . . . 5
1.10 Description of this Work . . . 6

2 Fabrication **7**
2.1 Fabrication Methods . . . 7
2.2 Device Characterization . . . 10
2.3 Fabrication Results . . . 10

3 Porosity and Micro/Nano Structure **12**
3.1 Density Measurements . . . 12
3.2 Carbon Nanotube Spacing . . . 13
3.3 Coated Carbon Nanotube Diameter . . . 19
3.4 Sidewall Carbon Capping . . . 24
3.5 Carbon Nanotube Morphology . . . 29

4 Cantilever Resonance Modeling **31**
4.1 Introduction . . . 31
4.2 Treating a Cantilever as a Simple Harmonic Oscillator . . . 32
4.3 Fitting Cantilever Resonance Data . . . 35

4.4 Cantilever Equation Solution 35
4.4.1 Definition of Variables 36
4.4.2 The Boundary Conditions 36
4.4.3 Separation of Variables 37
4.4.4 The Time Equation 37
4.4.5 The Spacial Equation 37
4.4.6 Applying Boundary Conditions 38
4.4.7 Substituting for the Separation Constant 40
4.4.8 The Final Solution 41
4.4.9 The Resonant Frequency 41
4.4.10 Resonant Modes 42
4.5 Adding a Linear Damping Term 44
4.5.1 The Resonant Frequency 44
4.5.2 The Effect of Damping with Respect to Geometry 45
4.5.3 Relating the Damping Coefficient to the Quality factor 45
4.6 Adding a Drive Term 45
4.7 Nonlinearities 46
4.8 Quadratic Drag 46
4.9 Timoshenko Beam Theory 46
4.10 Cantilever Relations 47
4.10.1 Stress-Displacement Relations 47

5 Resonance Testing **49**
5.1 Cantilever Mount and Drive 49
5.2 Cantilever Measurement 51
5.3 Nonlinearities 53
5.4 Multiple Resonant Modes 55
5.5 Resonant Frequency dependance on Geometry 55

6 Fluid Drag **57**

7 Sensing **61**

8 Modeling and Sensitivity Optimization **66**
8.1 Nomenclature 66
8.1.1 Design Variables 66
8.1.2 Intermediate Variables 67
8.1.3 Objective Function 67
8.1.4 Constants 68
8.2 Methods and Models 68
8.2.1 Constraints and Bounds 68
8.2.2 Gaussian Windowing 69

8.2.3 Surface Area vs Coating Radius . . . 70
8.2.4 Material Occupied Volume . . . 72
8.2.5 Device Density . . . 74
8.2.6 Device Elastic Modulus . . . 75
8.2.7 Resonant Frequency . . . 75
8.2.8 Damped Resonant Frequency . . . 76
8.3 Resonant Mode Shapes . . . 77
8.3.1 Hydrodynamic Function . . . 77
8.3.2 Reynolds Number . . . 79
8.3.3 Quality Factor . . . 79
8.3.4 Lorentzian Amplitude . . . 81
8.3.5 Sensitivity . . . 83
8.3.6 Optimization . . . 84
8.4 Results . . . 86
8.5 Optimization Conclusion . . . 92

9 Conclusion **93**
9.1 Future Work . . . 93

Appendix A Carbon Nanotube Growth Studies **95**

Bibliography **98**

Index **101**

List of Figures

2.1 Process diagram showing main fabrication and measurement steps 8

2.2 External SEM of a cantilever device 11

3.1 Plot of device density vs infiltration time 13

3.2 Device cross-section SEM showing porosity 14

3.3 FIB cut redeposition time lapse 15

3.4 FIB cut redeposition on a sample infiltrated for 3 minutes. 16

3.5 Sanded epoxy filled cross section indicating nanotube spacing 17

3.6 Cross section showing nanotube spacing 18

3.7 Capping is apparent on a the top of a sample infiltrated for 2 minutes 19

3.8 Top edge of a device infiltrated for 1 minute. 20

3.9 Broken middle of a 3 minute infiltrated sample 21

3.10 Inner coated carbon nanotube diameters at fill times of 1 to 6 minutes as indicated in the image 22

3.11 Cylindrical radius of coated carbon nanotubes is shown for various infiltration times 23

3.12 Sidewall views showing external nanotube coating diameter of a device infiltrated for 4 minutes. 24

3.13 Sidewall capping more prevalent near forest top 25

3.14 Broken cross section view of sidewall capping 25
3.15 Larger diameter coated nanotubes and some capping are apparent at the top of a sample infiltrated for 3 minutes 26
3.16 Visible capping at the top of a 5 minute infiltrated device. 27
3.17 CNT forest mas and height loss due to oxidation 28
3.18 Images of oxidized carbon nanotube forests 28
3.19 Twisting nanotube morphology at a device bottom 29
3.20 Straight nanotube morphology at a device center 30

4.1 Example plots of the simple harmonic oscillator solution 35

5.1 Cantilever measurement clamping schematic 50
5.2 Effect of driving voltage on resonance peaks 50
5.3 Effect of drive voltage on cantilever tip deflection 51
5.4 Resonance peaks indicating measurement reliability 52
5.5 Plot showing a typical resonance peak data set with a Lorentzian fit 53
5.6 Plot showing nonlinear effects: simulated 54
5.7 Plot showing nonlinear effects: measured 54
5.8 Multiple resonant modes 55
5.9 Length dependence of resonant frequency 56

6.1 Resonance peaks shown at three pressures 58
6.2 Resonant frequency shown to vary with pressure 58
6.3 Quality Factor shown to vary with pressure 59
6.4 Damping ratio shown to vary with pressure 59
6.5 Damping ratio pressure variation shows TED is not dominant 60

7.1 Histogram showing cantilever response to humidity 62

7.2 Equilibration between humidity levels 63
7.3 Cantilever resonance response to gas environment pressure 64
7.4 Initial attempt at sensing acetone vapor 65

8.1 Graph of surface area models created from circular assumption. 71
8.2 Plot of area occupied by the nanotubes in a horizontal cross-section. Comparing the circular intersecting model with the hexagonally close packed model. 74
8.3 Plot of the elastic modulus as a function of the porosity of the carbo-nanotube beam. 76
8.4 Plot of the deflection shape for each of the three first resonant modes of a cantilever beam 78
8.5 Assortment of plots showing the how changing each design variable will effect the quality factor of the beam 80
8.6 Concept diagram of quantitative cantilever sensitivity determination 84
8.7 Plot showing the change in sensitivity error over the life span of the particle swarm optimization 85
8.8 Plot showing the convergence for BFGS optimization sensitivity 86
8.9 Plot showing the relationship between the length of the beam and its sensitivity . . 87
8.10 Plot showing the relationship between the width of the beam and its sensitivity . . 88
8.11 Plot showing the relationship between the height of the beam and its sensitivity . . 89
8.12 Plot showing the relationship between the spacing of each nanotube and the beams sensitivity. 90
8.13 Plot showing the unconstrained relationship between the coating radius of the beam and its sensitivity. 90
8.14 Plot showing the relationship between the coating radius of the beam and its sensitivity. 91

A.1 CNT growth rate versus furnace placement position 96
A.2 CNT growth heights when the same substrate is used for multiple growths 96
A.3 Effect of total gas flow rate on CNT growth rate 97

List of Tables

4.1 The first ten constants governing cantilever bending behavior 40

4.2 Cantilever mode frequency constants 43

8.1 First four cantilever mode frequency constants 76

Chapter 1

Introduction

1.1 Cantilevers as Chemical Sensors

Micro-scale cantilevers (beams with one end held fixed and the other free to move) are commonly used as extremely accurate chemical detectors [1]. Detection can be achieved in one of two primary regimes: static deflection or resonance shift. In the static deflection method, one side of the cantilever is coated in a material that enhances the adhesion of the chemical to be sensed. When this coated cantilever is exposed to the chemical, molecules adsorb to the adhesion promoter, changing the surface stress on that side of the beam and causing the cantilever to bend. The amplitude of this deflection can then be measured and calibrated to the concentration of the desired chemical. In the resonance shift method, the entire cantilever is coated with an adhesion promoter, and the beam is driven into resonance. When this vibrating beam is exposed to the chemical of interest, molecules adsorb onto the surface of the cantilever, causing an increase in its effective mass and a resulting shift in resonance frequency. This resonance shift can be measured by means of several methods such as laser deflection or capacitative current.

The use of micro-cantilevers as chemical sensors is a powerful technique [1]. Utilizing pro-

cesses from the semiconductor industry, these devices can be mass produced at low cost. In addition, small device size allows for sensors to be easily incorporated into many systems. Since the micro-cantilever sensing method is not inherently dependent on the chemical to be sensed, large arrays of cantilevers can be fabricated in which each beam receives a different coating. The array can then provide simultaneous information on the concentration of many chemicals, becoming a "chemical nose" [2].

Although other chemical sensing methods may compare favorably in some respects, micro-cantilever sensing often offers advantages. An example is provided by quartz crystal microbalance (QCM) based sensing. This method has become popular across many fields due to its ease of use and high fidelity. While this method has become somewhat of a standard for single chemical sensing, the large detector size has limited its use in parallel sensing applications, and the overall cost of the method can be significantly higher than that of micro-cantilever based sensing.

1.2 Successes of Current Devices

Current solid cantilever based sensors are very successful. Extremely high sensitivities have been achieved. One source reports an acheived mass sensitivity of seven zeptograms [3], or the approximate mass of twenty gold atoms.

Parallelization has been realized in current cantilever sensors. Large arrays have been made, allowing for many measurements to be performed simultaneously.

A great deal of work has gone in to exploring various coatings. If each cantilever in an array is modified with a distinct coating, then each beam will be primarily sensitive to separate substances, forming a chemical nose. Success has been found in designing coatings with high selectivity. In addition, various methods of coating application have been explored.

1.3 Limitations of Current Devices

Nearly all micro-cantilever sensors created as of the time of writing are solid devices , frequently made of solid silicon-based materials such as silicon or silicon nitride. Although a few devices have been made with increased surface roughness or a surface porous layer, fully porous devices have not been well explored.

With a solid cantilever sensor, the device density is fixed by the chosen material. In order for the mass of the cantilever to not become excessively larger than the mass of the analyte and overpower it in the measurement, solid cantilever sensors must resultingly be made very thin. Thin cantilevers, however, suffer from low quality factors in fluid environments due to the small amount of energy in their resonant mode. As a result, solid cantilevers generally can only obtain high quality factors and sensitivities in vacuum. When a solid cantilever sensor is exposed to air or liquid, sensitivity drops drastically.

Solid cantilevers have faced limitations in many desireable arenas, as the majority of chemical sensing applications necessitate measurement in gas or liquid.

1.4 Advantages of Porous Cantilevers

Porous devices have much higher surface areas than their solid counterparts. It is common for a porous cantilever to have a surface area three orders of magnitude higher than a solid cantilever of the same dimensions. Since sensitivity of a cantilever resonator is roughtly proportional to the surface area of the beam available for adsorption, this increase in surface area could have a large impact on sensitivity.

For a solid cantilever , the ratio of surface area to volume decreases quickly with an increase in any dimension of the beam. For a fully porous cantilever with continuous pores, this ratio is independent of geometry. Since the analyte mass is proportional to cantilever surface area and the

cantilever mass is proportional to its volume, the neccessity of maintaining a favorable mass ratio (the ratio of the mass of the analyte to the mass of the cantilever) leads to stringent constraints on the mass of a solid cantilever that do not apply to a porous cantilever sensor. As a result, a porous cantilever can be designed to have a higher quality factor in fluid environments than a solid cantilever. This allows porous cantilever sensors to be used in environments that pose great difficulty to solid cantilever sensors.

1.5 Potential Disadvantages of Porous Cantielvers

Concern has been expressed that a porous material would experience large amounts of thermoelastic dampening (TED) that would cause energy loss and a decrease in quality factor. For resonant cantilever sensors designed to be used in fluids, fluid damping is likely large. Increased TED for a porous sample is not a concern if fluid damping remains dominant.

1.6 Previous Work on Porous Sensors

As the advantages of porosity in resonant sensors has been realized, several attempts have been made to take advantage of this property [4]. One approach has been to increase the surface roughness of a solid structure, leading to an approximate factor of two increase in surface area. Another approach has been to fabricate devices with a thin porous layer atop a solid structure. This has greatly increased the surface areas and resulting sensitivities of these sensors.

1.7 Limitations in Current Microfabrication Processes

Unfortunately, current microfabrication processes are not generally compatible with porous materials. Techniques that have been explored for the fabrication of porous micro-scale devices have

found success mostly only in low aspect ratio regimes . In addition, most methods used to date form isolated pores that do not provide diffusion paths through the entire structure.

1.8 Review of the CNT-M Process

The carbon nanotube templated microfabrication (CNT-M) process allows for full porous devices to be fabricated on the microscale with high aspect ratios. This method allows for devices to be realized with finely tunable porosity, and in a diverse range of materials [5].

In brief, the process relies on the vertical growth of carbon nanotubes from a micro-patterned iron catalyst. After these carbon nanotubes have been synthesized, extruding the two dimensional shape defined by the iron, the nanotubes can be coated in other materials. This other material of choice infiltrates the structure, beginning to fill the interstices between carbon nanotubes. The infiltration process can be continued until a solid device is obtained, or stopped to leave a structure with controlled porosity.

1.9 Advantages of the CNT-M Process

The CNT-M process provides a versatile and scalable microfabrication method. There are several relavant advantages to this technique. Firstly, the final device porosity is easily altered by changing the process' infiltration time. Not only can this process form a porous device, but the method naturally lends itself to devices with largely continuous and often connected pores, providing long diffusion paths that can even extend through the entire device. Secondly, this method is capable of producing devices with ultra-high aspect ratios. For example, while competing high aspect ratio processes such as reactive ion etching (RIE) struggle to reach aspect ratios above 20, CNT-M easily acheives aspect ratios above 200. For cantilever sensors, a high aspect ratio fabrication technique allows cantilevers to be made thick in the direction of motion, increasing quality factor in fluids.

Thirdly, where other high aspect ratio microfabrication methods are highly material dependant, CNT-M defines geometry independant from material, allowing for cantilever sensors to be created from many materials using a single overarching method.

1.10 Description of this Work

Here we present the fabrication of porous cantilever sensors using the CNT-M process. We show characterization and modeling of the device micro and nanostructure, including pore size, density, nanotube spacing, and coating diameters for various infiltration times. We show solution of cantilever partial differential equations, including the development of a damping term and resulting relations. We show the characterization of the resonant characteristics of these cantilevers, confirming models and exploring behavior. We show cantilever behavior across pressures and in different environments, demonstrating the behavior of fluid damping and showing that Thermo Elastic Dampening (TED) is not dominant even in atmospheric air conditions. We present use of these cantilever beams as sensors employed in sensing water and acetone vapors down to ppm levels in the case of the former. We also present numerical optimization of cantilever sensor properties based upon the developed model.

Chapter 2

Fabrication

2.1 Fabrication Methods

To begin the fabrication process, a silicon wafer was coated with 30 nm of aluminum oxide (alumina) by electron-beam evaporation. This coating acts as a diffusion barrier later on during the carbon nanotube growth portion of the fabrication process. Subsequently, standard optical lithography techniques are used to pattern approximately 1 μm of positive photoresist onto the substrate. A 4 nm thick iron film was then deposited onto the sample by thermal evaporation. This procedure was a line-of-sight deposition technique, such that metal was left either directly on the substrate or on top of photoresist. When the sample was removed from the vacuum chamber of the thermal evaporator, the iron was quickly oxidized under ambient conditions. Subsequently, the photoresist was removed by sonication in n-methyl pyrolidone (NMP). As the photoresist dissolves it lifts off the iron oxide on its surface. When the sample was taken out of solution, only iron oxide that was initially deposited directly onto the alumina coated silicon substrate remains, forming a desired pattern.

Carbon nanotube growth was the next phase of the fabrication process. The sample was first

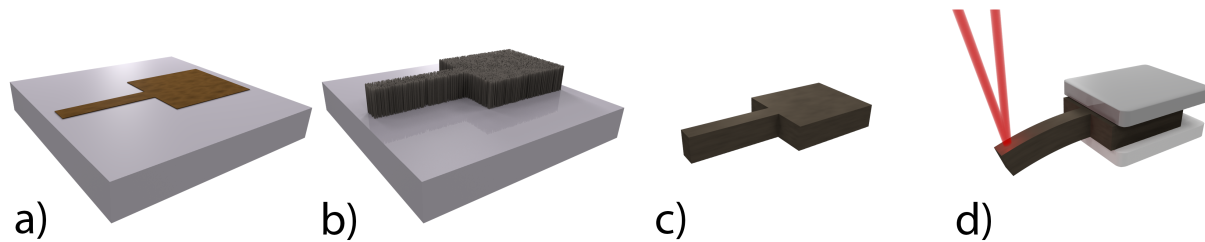

Figure 2.1 A process diagram showing the main fabrication and measurement steps. a) Iron is patterned onto an alimina coated silicon substrate using standard optical photolithography, b) carbon nanotubes are grown from the iron catalyst, c) nanotubes are coated in a filler material and the device is removed from the substrate, d) the base of the device is clamped to a piezoelectric drive and laser deflection is used to measure vibration amplitude.

heated in a tube furnace under a 230 sccm flow of hydrogen gas . As the furnace heats the sample, the hydrogen gas reduces the iron oxide back to iron metal . The iron becomes increasingly mobile on the surface as the temperature rises. Although all temperatures remain well below the melting point of bulk iron metal, it should be noted that not only could this largely surface iron have properties differing largely from the bulk, but also that the nature of metalic bonding allows for significant thermal mobility in the solid state at small scales. As a result, the iron film dissociates into nanoparticles on the alumina surface .

When the furnace reaches a temperature of 750 °C, a flow of 230 sccm of ethylene gas was added to the previously flowing hydrogen gas. The ethylene gas provides a source of carbon for the carbon nanotube synthesis . When ethylene molecules come into contact with iron nanoparticles, the iron catalyzes their decomposition. This leads to mobile carbon atoms on the surfaces of the iron nanoparticles. These carbon atoms have enough thermal energy to covalently bond together, forming chains and rings on the surface of the iron catalyst particles. As this process continues, a carbon nanotube begins to form, with new carbon atoms being added to the structure at the nanotube/iron interface. This results in what was commonly described as the “growth” of carbon nanotubes from iron catalyst “seed” particles such that the nanotubes then form a “forest.” The length of the carbon nanotubes and resulting height of the forest can be controlled by the amount

of time ethylene gas was flowed over the substrate at 750 °C.

Once the carbon nanotubes have been synthesized, the interstices between them can be infiltrated with other materials in order to form a more robust structure. The nanotubes are not initially bound to one another by any means other than Van Der Waals forces. By coating the outer surface of each carbon nanotube with another material, however, each juncture where one nanotube touches another can be locked by the coating material. This allows a forest of disconnected carbon nanotubes to be joined into a single structure. If the nanotubes are coated with a thin layer of material, or in other words if the interstices between nanotubes are filled to a small degree, then an extremely porous structure can result . As filling continues, the pores in the composite material will become smaller until a nearly solid structure was obtained.

There are many materials that could potentially act as filler materials in this process. Conceivably any material that can be deposited by means of chemical vapor deposition (CVD) could be used. Our group has successfuly explored several of these materials, such as carbon, nickel, copper, tungston, silicon, silicon dioxide, silicon nitride, and others. [6]

This study primarily utilizes carbon as a filler material due to its ease of deposition. After carbon nanotubes have been grown, the hydrogen and ethylene gas flows are replaced by an inert argon flow while the furnace was heated further to 900 °C. When this temperature was reached, gas flow was toggled back to the hydrogen/ethylene combination. Gas flow was continued at the stated temperature for the desired infiltration time. At this heightened temperature, ethylene molecules no longer need a catalyst to decompose. As a result, the molecules decompose readily throughout the chamber, depositing carbon onto all exposed surfaces. When the desired infiltration time was reached, gas flow was switched to argon to flush the hydrogen and ethylene while the sample was cooled back to ambient temperature in an inert atmosphere.

The sample can be mechanically removed from the substrate or etched to release it.

2.2 Device Characterization

The height of each device was directly measured by means of a micrometer. After being removed from the silicon substrate, each device was placed in the measurement gap of a micrometer. The micrometer was then tightened until it reaches its first force setpoint (the outer knob clicks once and disengages).

A scanning electron microscope (SEM) was used to image the exterior of the devices after fabrication.

2.3 Fabrication Results

The fabrication process was flexible over a large range of length scales. In this study, cantilevers were fabricated with lengths ranging from 100 μm to 10 mm, widths ranging from 50 μm to 2 mm, and heights ranging from less than 10 μm to almost a milimeter. These fabricated devices span at least two orders of magnitude in scale, and the fabrication process in not bounded on any of the stated extremes except that the hight was nearing a limit of approximately 3 mm. The other dimensions could easily be made either larger or smaller as desired with no real change in the method.

High aspect ratio devices are easily obtainable with this fabrication process. Typical sidewall straightness and device thickness can be seen in Figure 2.2.

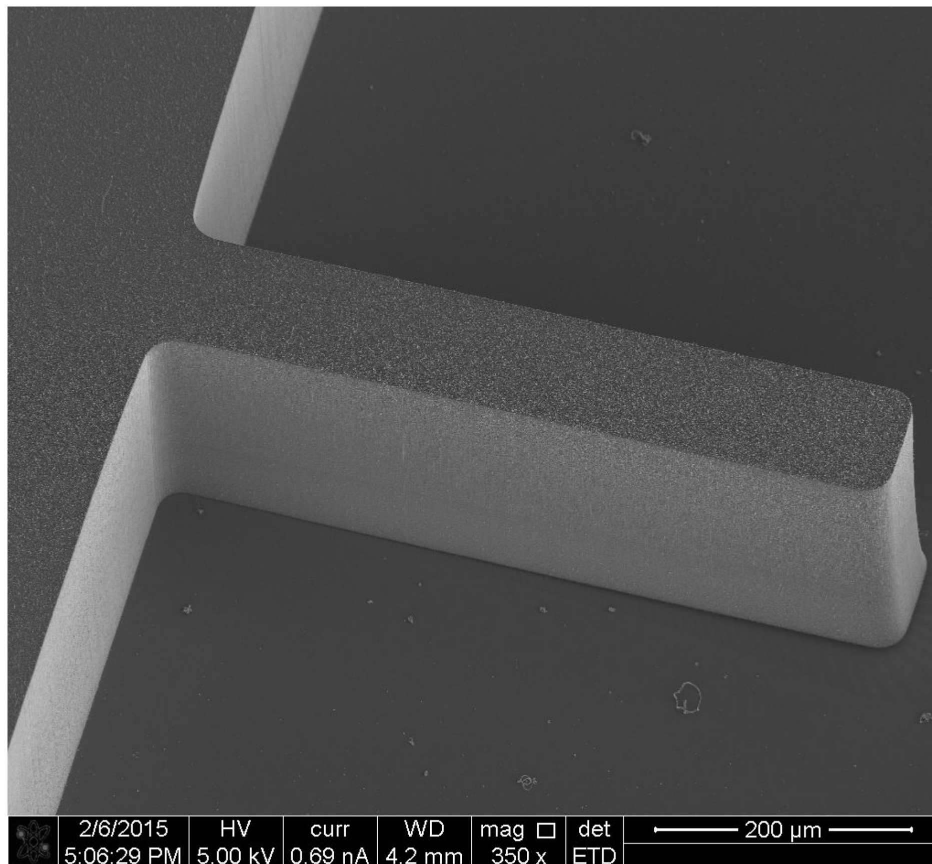

Figure 2.2 External image of a device obtained by SEM.

Chapter 3

Porosity and Micro/Nano Structure

Since both the microstructure and the nanostructure of these cantilevers strongly influences their sensing behavior, a careful characterization of these properties follows in the current chapter.

3.1 Density Measurements

The porosity of the device material can be controlled through the time for which the structures are infiltrated with a filler material. This variable porosity can be observed indirectly through a variable density of the resulting device. Densities obtained using carbon as the filler material can be seen in Figure 3.1 to range from less than 100 kg/m^3 to more than 1000 kg/m^3.

The mass of each device was determined by use of a microbalance. To improve accuracy, the substrate with the device attached was first placed on the balance and the mass recorded. The device was then removed from the substrate. Afterward, the substrate mass was determined once more. In some cases, the device itself was then placed alone on the balance to determine its mass directly. In general, however, the difference in mass of the substrate before and after device removal proved a more robust measurement method as some devices were damaged in the course of removal, altering their mass.

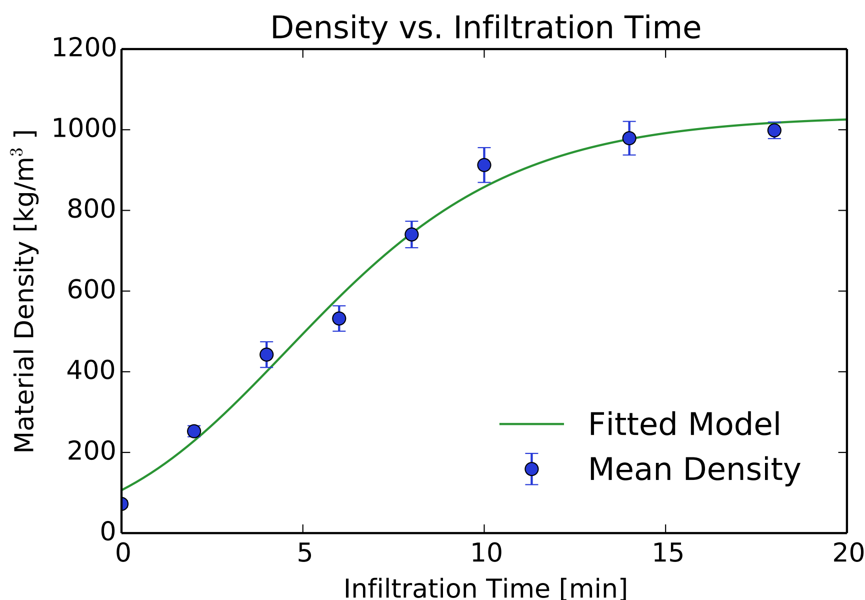

Figure 3.1 The overall device material density is plotted against the time for which the device was infiltrated. The filled dots represent the mean of several data points, while the error bars indicate one standard deviation on each side of the mean. A model for the infiltration process is also shown. The details of the derivation of this model can be found in the text.

Since the in-plane area of each device was known from the geometry defined by the photolithography mask, the height was known by micrometer measurements, and the mass was known from the microbalance result, the device density can be computed. The porosity of the devices can be estimated from the device density.

3.2 Carbon Nanotube Spacing

Device porosity can also be measured directly. A focused ion beam (FIB) was first used to cut into the side of a device, milling material away. Afterward, the device cross section cut by the FIB was imaged by SEM. Images obtained by this method should more directly show the pore sizes and filling fraction of the porous device.

Due to the nature of the aligned carbon nanotubes being used as the basis to create a porous structure, the resulting pores in the material were observed to be generally aligned and continuous. This can be seen from the cross section in Figure 3.2. Porous materials most commonly have a large fraction of pores that are isolated from other pores and the external environment. The nature of this carbon nanotube scaffolded process is observed to create a large fraction of continuous pores that are not isolated.

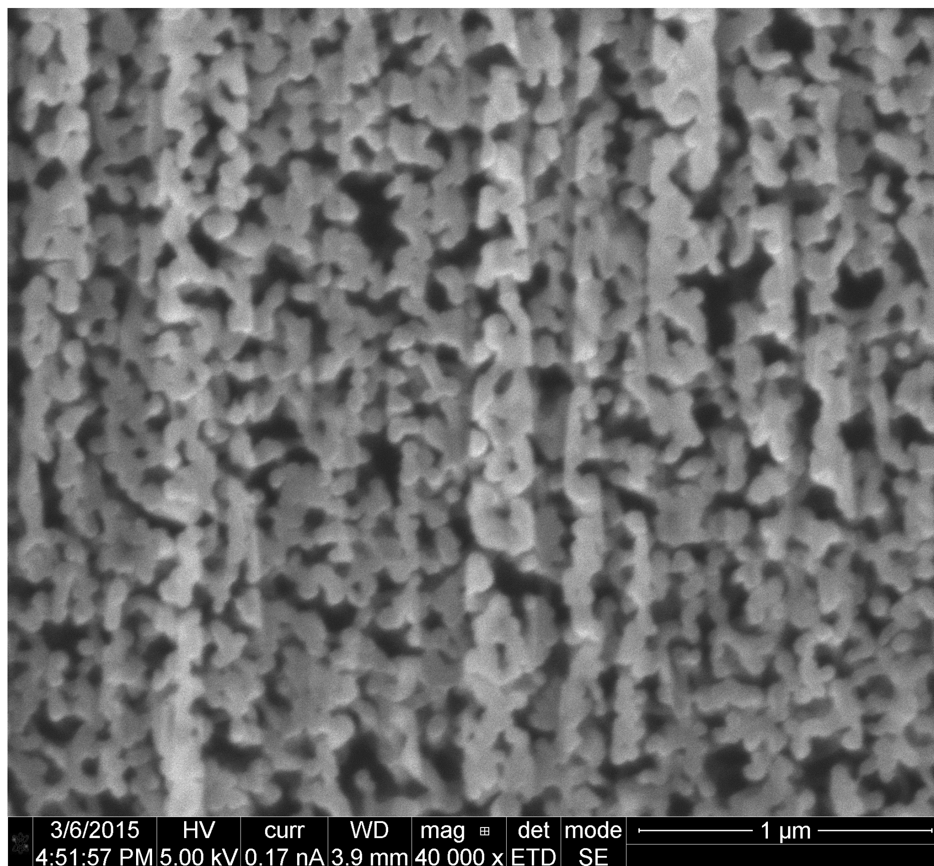

Figure 3.2 A cross section of the device material showing the degree of porosity and pore size. Cross section obtained by FIB milling and imaged via SEM.

This method, although more direct than measuring overal device density, faces several challenges. The most important of these challenges is redeposition. When milling, sanding, or otherwise creating a cross section in a porous material, removed material may redeposit into the pores,

altering the porosity measurement. The process of redeposition can be clearly seen in Figure 3.3. This figure shows a time lapse of a milling FIB cut. When the beam first opens an area, some pores can be seen. As the cut continues, however, those pores vanish as newly milled material redeposits into previously opened pores.

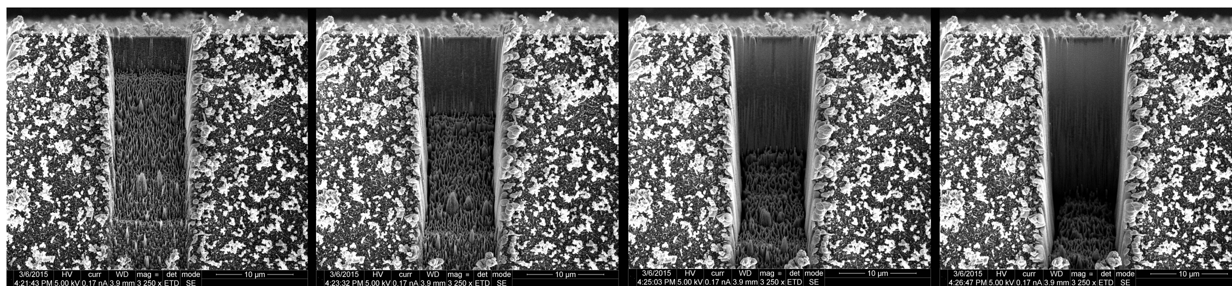

Figure 3.3 Time progression from left to right of a FIB cut being made into a device infiltrated for 3 minutes. It is clear that redeposition is filling in exposed pores, preventing a reliable estimate of porosity or nanotube spacing.

When the cut is complete, no pores remain to be imaged, as can be seen in Figure 3.4. This image shows a smooth, almost polished surface that is the plane of the FIB cut seen in Figure 3.3. When milling in this way, it is desireable to leave a smooth surface for imaging. Creating such a smooth surface requires extra passes of the ion beam along that surface, but these extra passes also promote redeposition. When these extra passes are omitted, a phenomenon called curtaining results. This effect can be seen in Figure 3.3, where it is clear that the imaged surface is not smooth, but resembles a curtain hung from the top of the page. By making a quick and rough cut such as this, the pores can be imaged, but pore sizes cannot be estimated reliably by this method because they are altered by the cutting process.

What can be measured by this technique, however, is the average distance between carbon nanotubes, or the distance between centers of the coated carbon nanotube posts seen as circles in the cross section. While Figure 3.3 can give some indication of what this distance is, it quickly becomes clear that depth of the pores creates uncertainty as to what features are actually on the plane of interest.

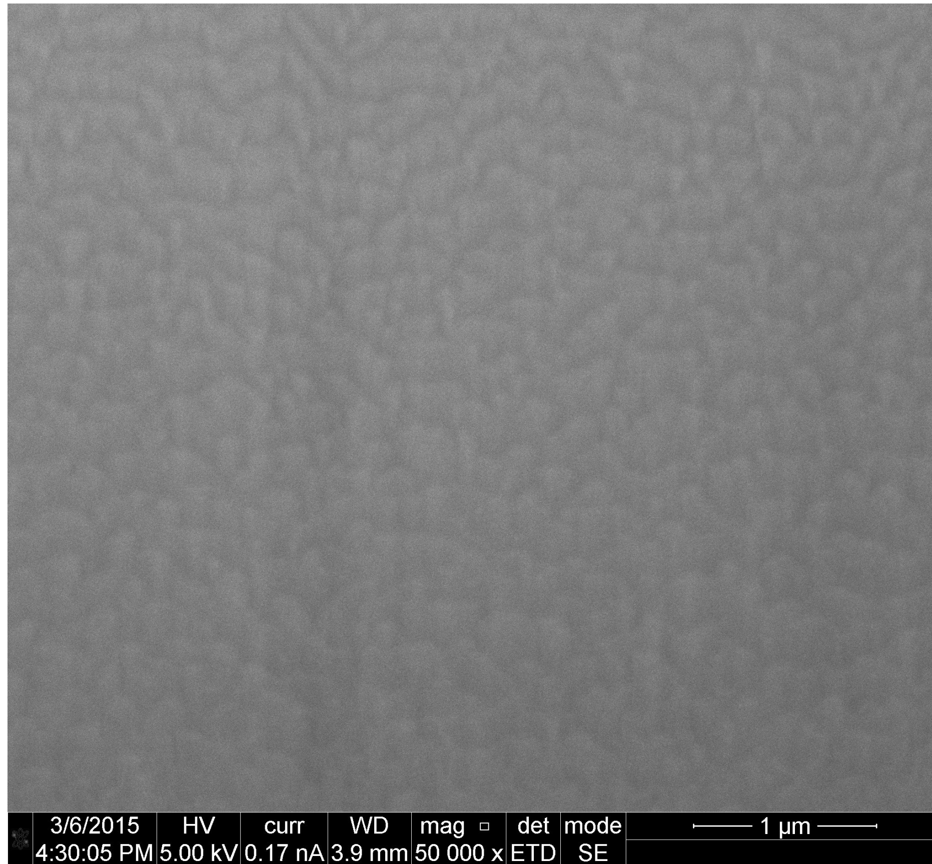

Figure 3.4 FIB cut redeposition on a sample infiltrated for 3 minutes.

Both the problem of redeposition and the difficulty in determining what features lie on the cross sectional plane can be avoided by filling the pores prior to cross sectioning the device. One approach is to fill the pores with epoxy resin. This was done, using the epoxy M-Bond. After the epoxy was cured, the sample was cross sectioned using abrasive mechanical TEM (Transmission Electron Microscopy) sample preparation techniques. The imaged cross section obtained by this method is shown in Figure 3.5.

This approach yeilds a better estimation of nanotube spacing, but the similarity between the epoxy material and the coated carbon nanotubes as well as the poor conductivity of the epoxy result in poor image quality.

To improve overall sample conductivity and provide greater contrast between coated carbon

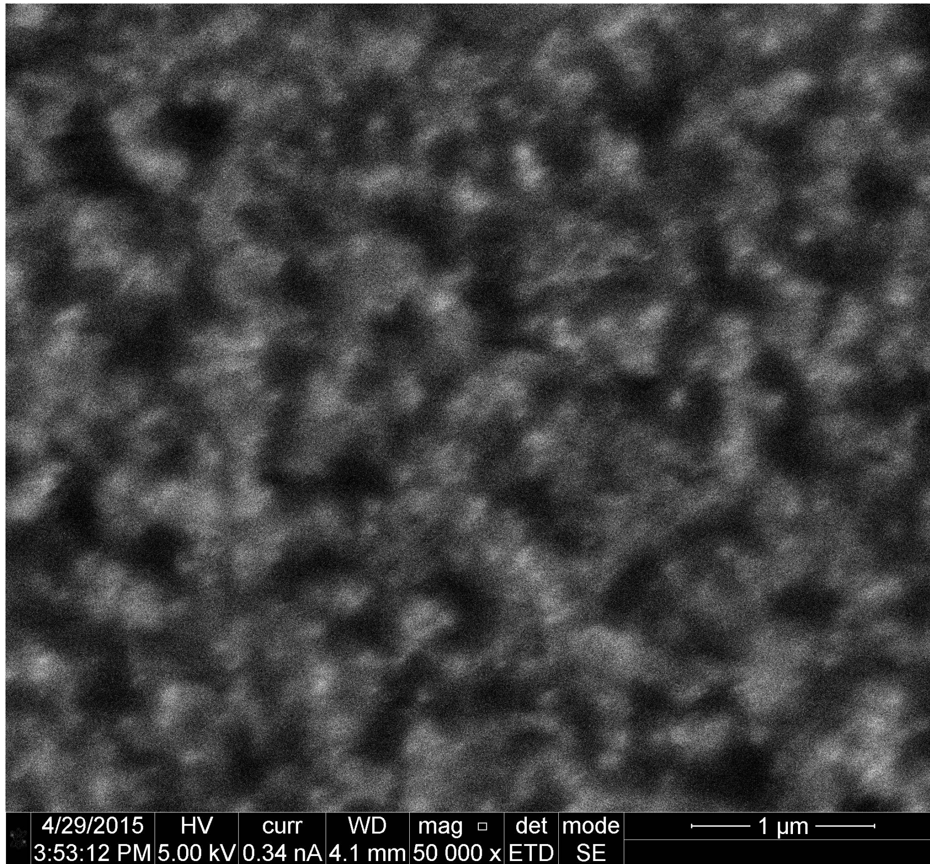

Figure 3.5 Imaged cross section perpendicular to nanotube growth direction giving an indication of nanotube spacing. This sample was grown using 4 nm thick iron catalyst, infiltrated for 2 minutes, impregnated with epoxy resin (M-Bond), cross sectioned using mechanical abrasive TEM sample techniques, and imaged with the image plane parallel to the cross sectional plane. Excess charging and limited contrast between epoxy and carbon coating degraded this measurement.

nanotubes and filling material, the pores can be electroplated with nickel following the process of Barrett et al [7]. This approach proved much more reliable than the previously described methods, and the result can be seen in Figure 3.6.

The sample pictured in Figure 3.6 was fabricated with a 7 nm thick iron catalyst. Most cantilever samples in this study used 4 nm thick iron catalyst. It is known that catalyst thickness influences carbon nanotube spacing. Future work will include nickel plating and cross sectional imaging of a 4 nm iron catalyst sample. Figure 3.5 as well as all other figures with the exception

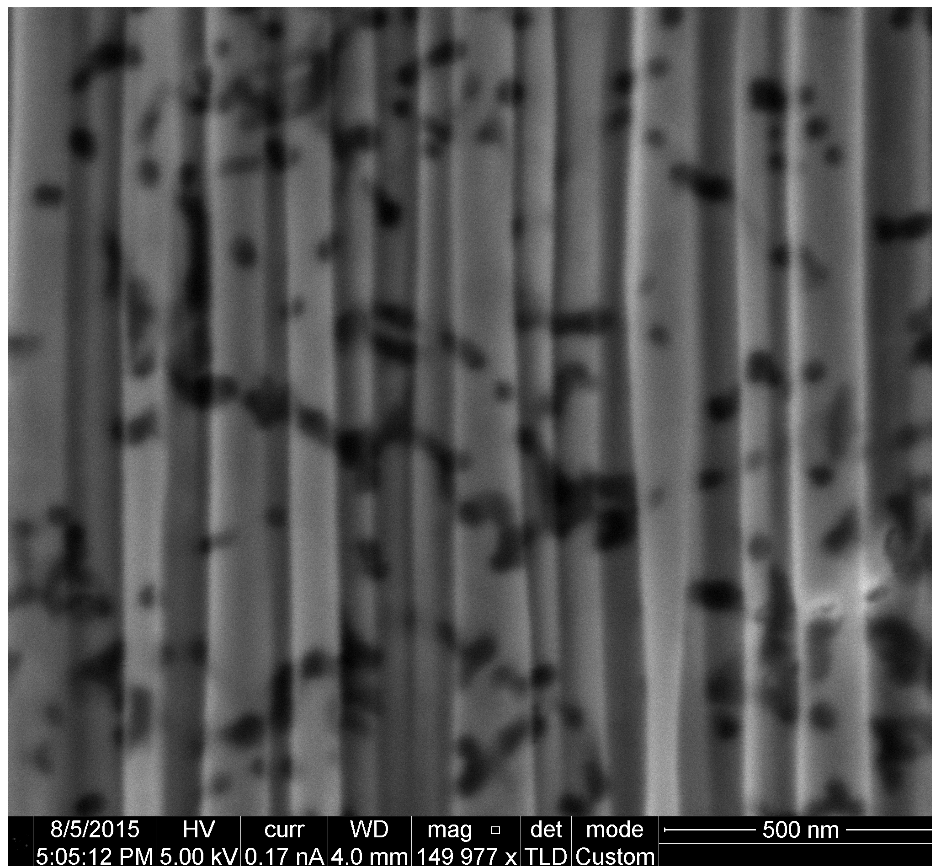

Figure 3.6 A cross section of a nickel filled device center cut and imaged perpendicular to the nanotube growth direction. Dark circles are coated carbon nanotubes. This cross section gives a reliable estimate of carbon nanotube spacing. Some curtaining is visible from the FIB cut (vertical lines). This sample was grown with a 7 nm iron catalyst.

of Figure 3.6 represent samples with 4 nm thick iron catalyst.

3.3 Coated Carbon Nanotube Diameter

Alongside the average distance between neighboring carbon nanotubes, the other parameter that largely influences pore size and porosity is the diameter of the coated carbon nanotubes. This diameter is very different on the outside of a device than on the inside, as can be seen in Figure 3.7. This figure shows a broken cross section displaying the top edge of a device.

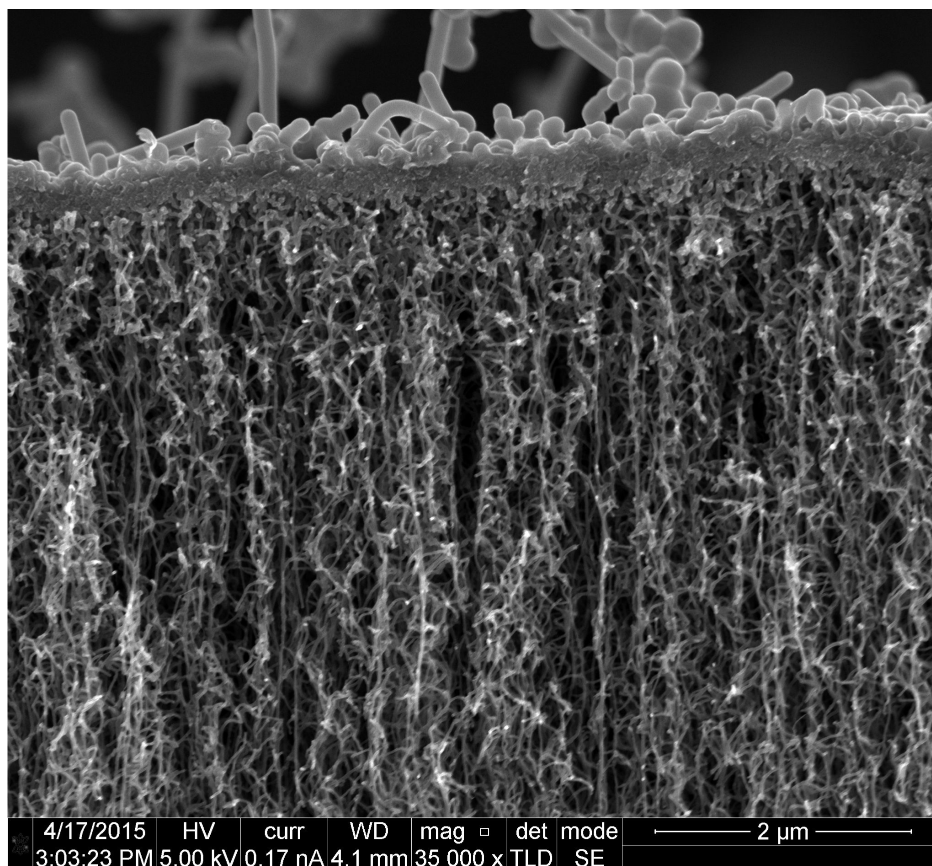

Figure 3.7 Capping is apparent on a the top of a sample infiltrated for 2 minutes

It is clear that the coated carbon nanotube diameter at the top of the image is very different from that at the bottom. Resultingly, images such as Figure 3.8 that are taken looking at a structure from the outside say little about the coated carbon nanotube diameter inside the structure.

Because diameter can vary at different locations on a structure, it is desirable to image device

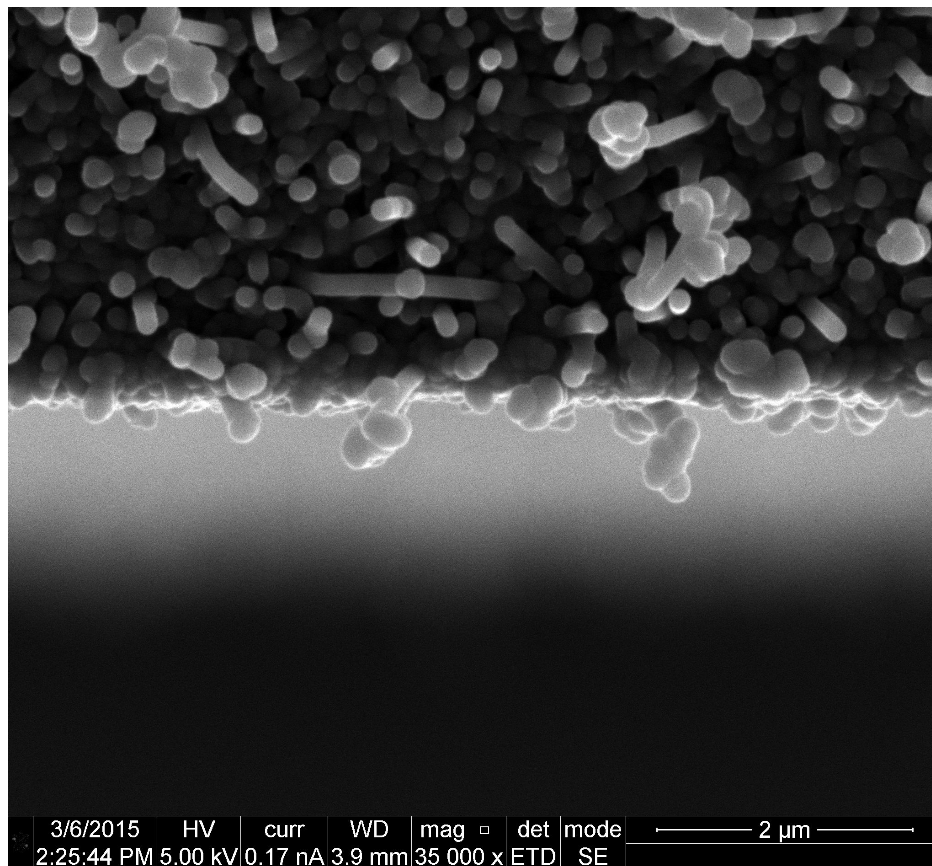

Figure 3.8 Top edge of a device infiltrated for 1 minute.

cross sections in order to view inner structure coating diameters. As a result of all the difficulty in making clean cross sections that avoid redeposition as discussed above, cross sections for diameter measurements were made by cleaving samples in planes parallel to the average carbon nanotube growth direction. Using this breaking method, images such as Figure 3.9 can be obtained, yeilding an accurate measurement of coated carbon nanotube diameter.

Similar images were taken for samples that were infiltrated for different amounts of time. A sampling of these images can be seen in Figure 3.10.

One hundred coated nanotube diameter measurements were made on each of three replicates of each infiltration time. The measured coated carbon nanotube diameters are summarized in Figure 3.11.

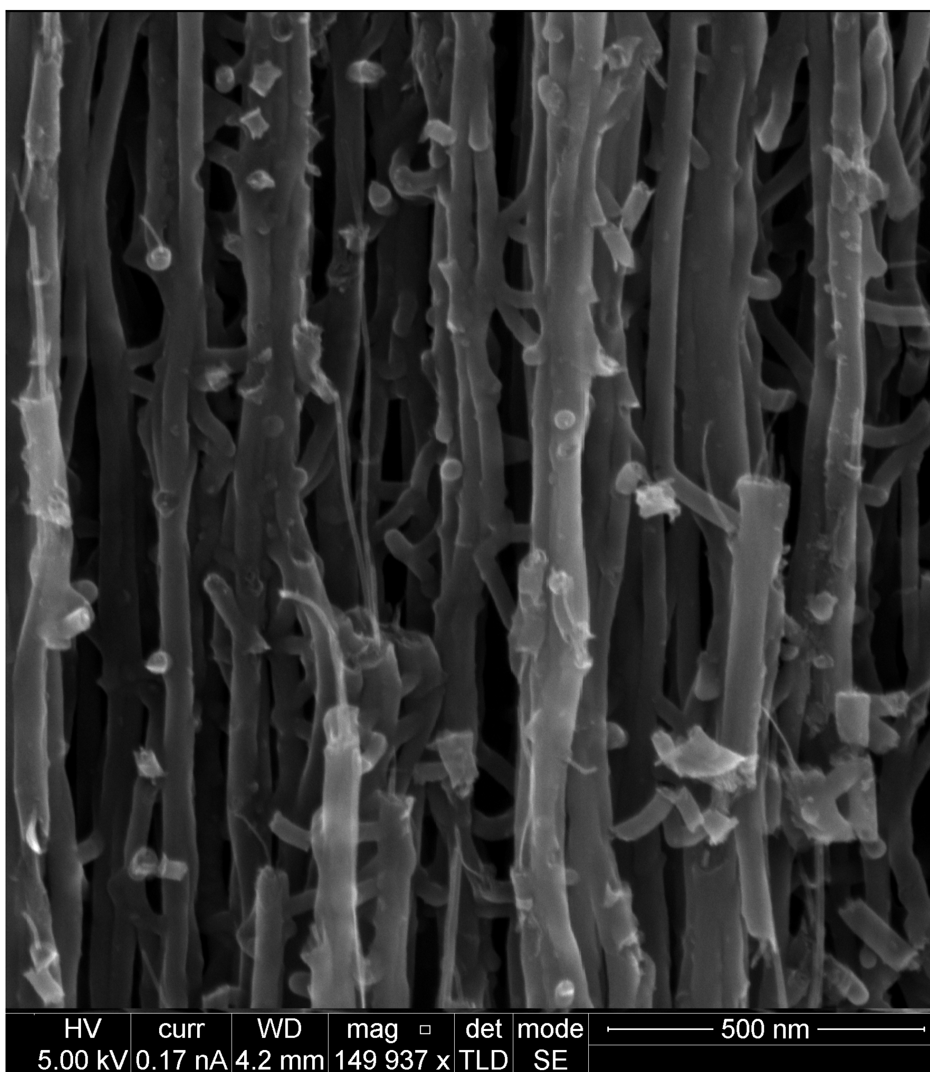

Figure 3.9 Broken middle of a 3 minute infiltrated sample

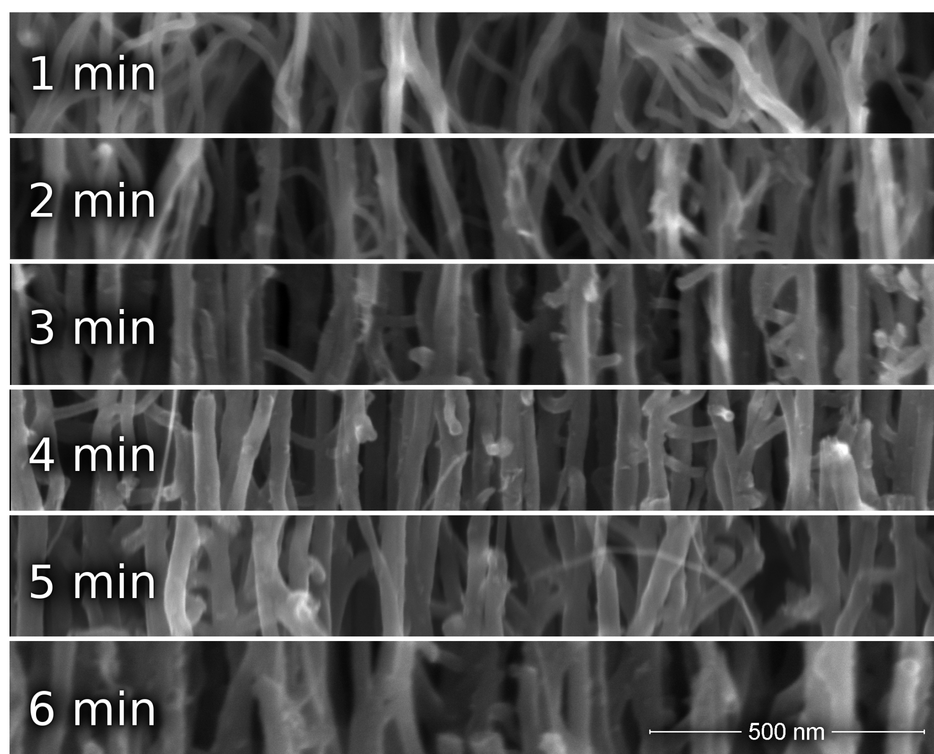

Figure 3.10 Inner coated carbon nanotube diameters at fill times of 1 to 6 minutes as indicated in the image

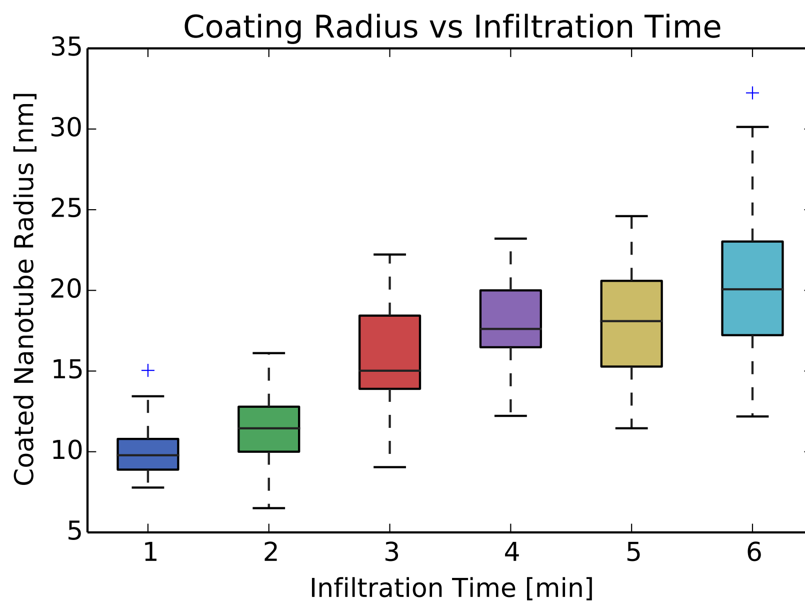

Figure 3.11 Cylindrical radius of coated carbon nanotubes is shown for various infiltration times

3.4 Sidewall Carbon Capping

The observation that coated carbon nanotube diameter varies largely with location in the sample and gets larger near the edges raises some concern. For a porous cantilever sensor to be effective, there must be diffusion paths from the outside to the inside of the porous structure. If a structure becomes capped by a nearly solid shell during fabrication then it may not preform well as a sensor.

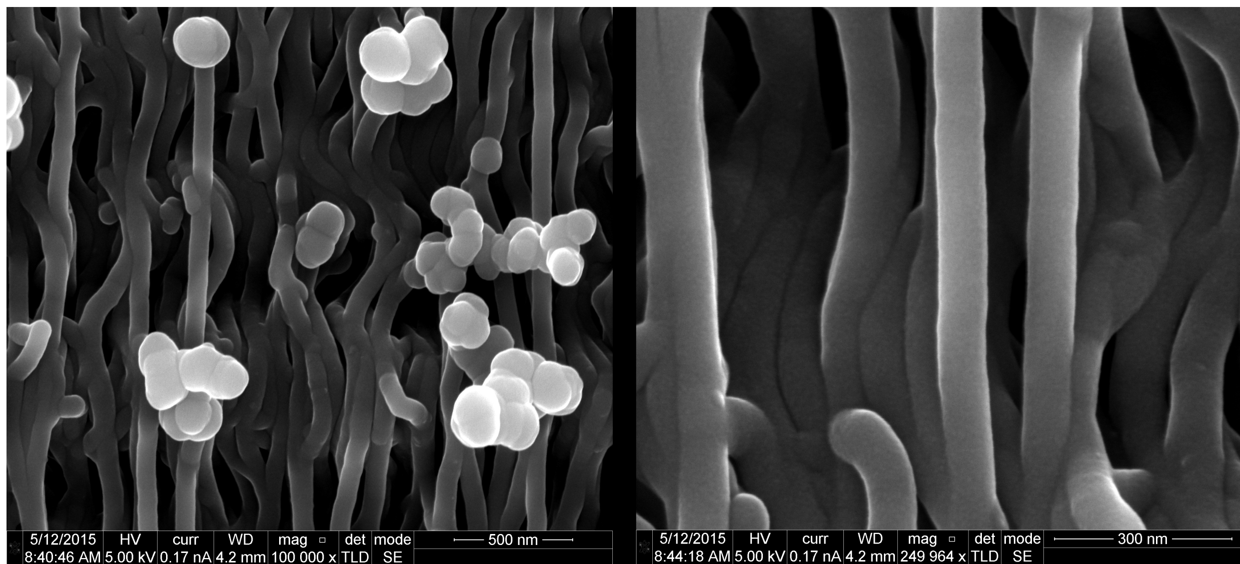

Figure 3.12 Sidewall views showing external nanotube coating diameter of a device infiltrated for 4 minutes.

Figure 3.12 shows a view of a device sidewall that has not been broken open. This is an external surface that could potentially be capped with infiltration material. The figure is not conclusive in any sense, but there is definitive depth to the image, suggesting that external porosity is maintained and diffusion paths exist.

In Figure 3.13, however, we see two views similar to that of Figure 3.12, except that one is taken near the middle of the height of a sample while the other is at the top edge. The image near the top does not suggest diffusion paths as strongly as the image in the middle of the structure.

A more definite indication is given by Figure 3.14, which shows a broken cross section in the

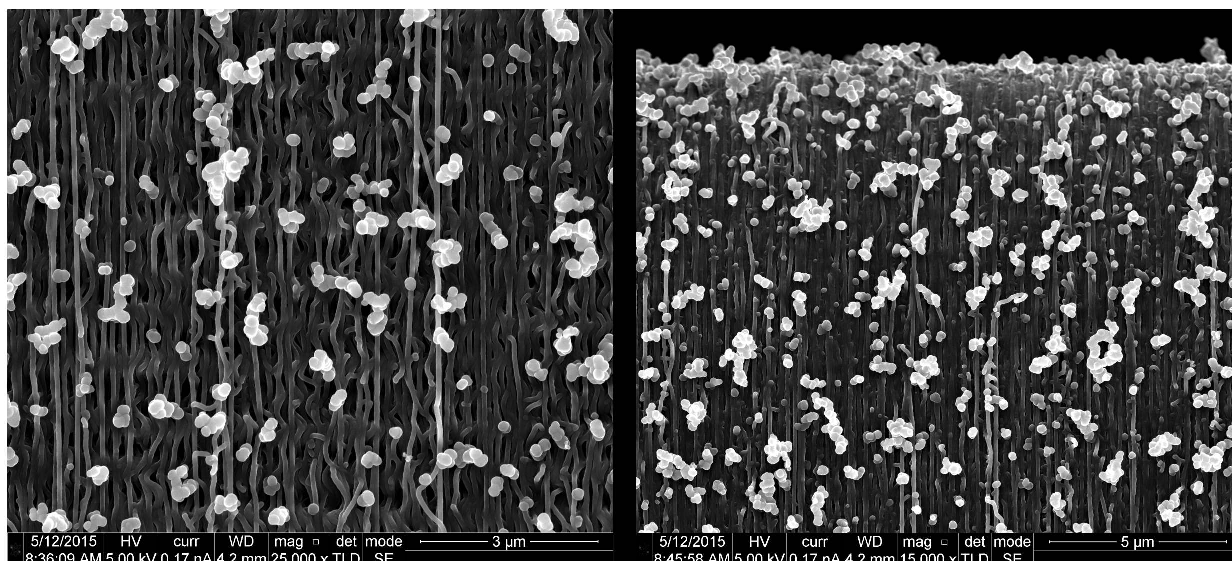

Figure 3.13 Two images showing the middle (left) and upper (right) sidewall of the same device. Qualitatively these images suggest that there may be more sidewall capping near the top of a device infiltrated for 4 minutes.

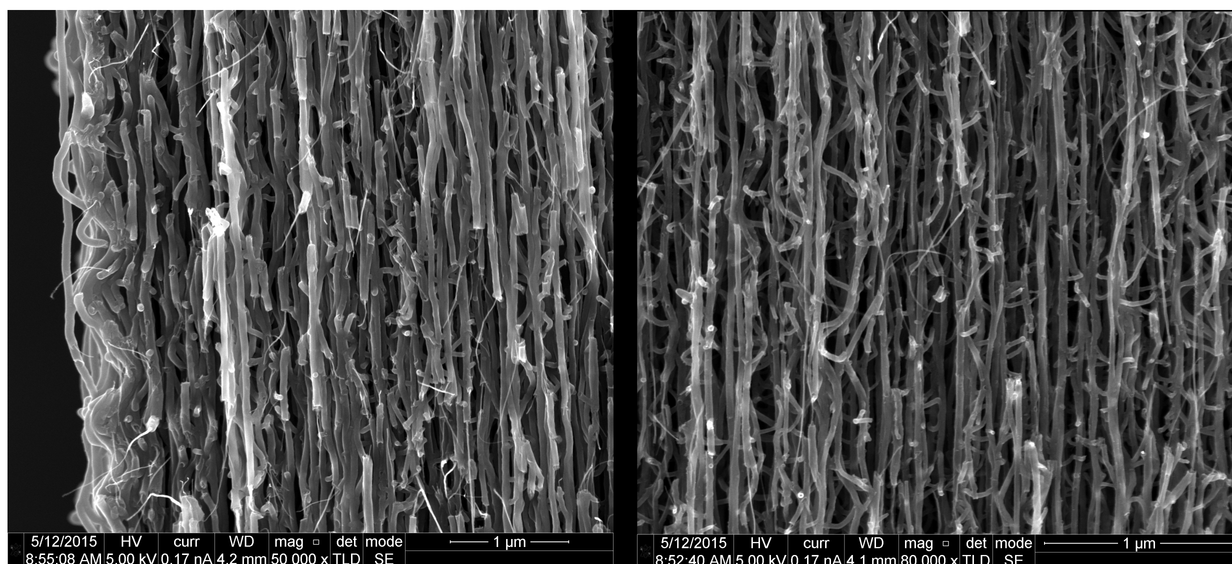

Figure 3.14 Two views of one 4 minute infiltrated device that has been broken open to provide a cross section. Coated nanotubes near the device edge (left) have larger diameters than those near the device center (right), and some sidewall capping is visible.

middle and at an edge of a sample. Here it is seen that the diameters are larger near the edge of the device, but it does appear that diffusion paths still exist.

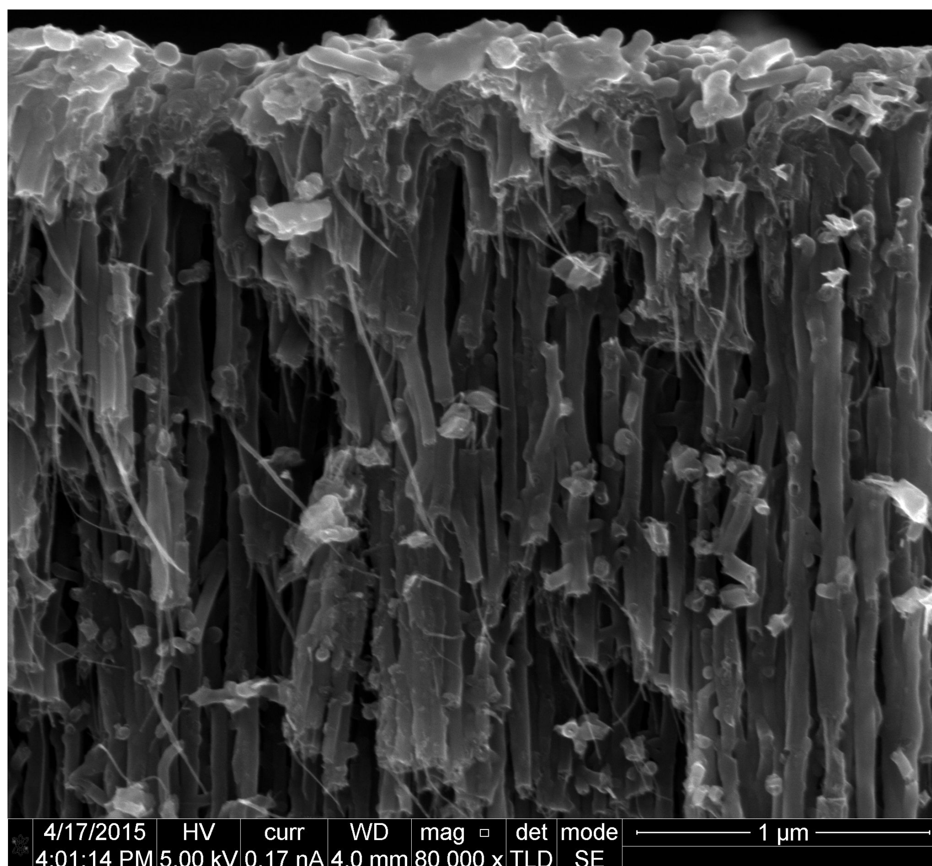

Figure 3.15 Larger diameter coated nanotubes and some capping are apparent at the top of a sample infiltrated for 3 minutes

Figure 3.15 shows that capping becomes a larger problem near the top of devices than it does along the external sides.

Figure 3.16 shows that after only 5 minutes of infiltration, capping is becoming a concern. For cantilevers studied, diffusion paths have existed. If capping begins to limit cantilever function as a sensor, excess infiltration material could be removed or limited during growth, such as by heating the sample in a low concentration of flowing water vapor in the case of carbon infiltration.

Figure 3.17 shows an initial exploration related to this potential solution. In this study, grown carbon nanotube forests were afterward massed and exposed to a flow of 230 sccm hydrogen gas bubbling through water vapor at various temperatures for 30 minutes. The samples were then

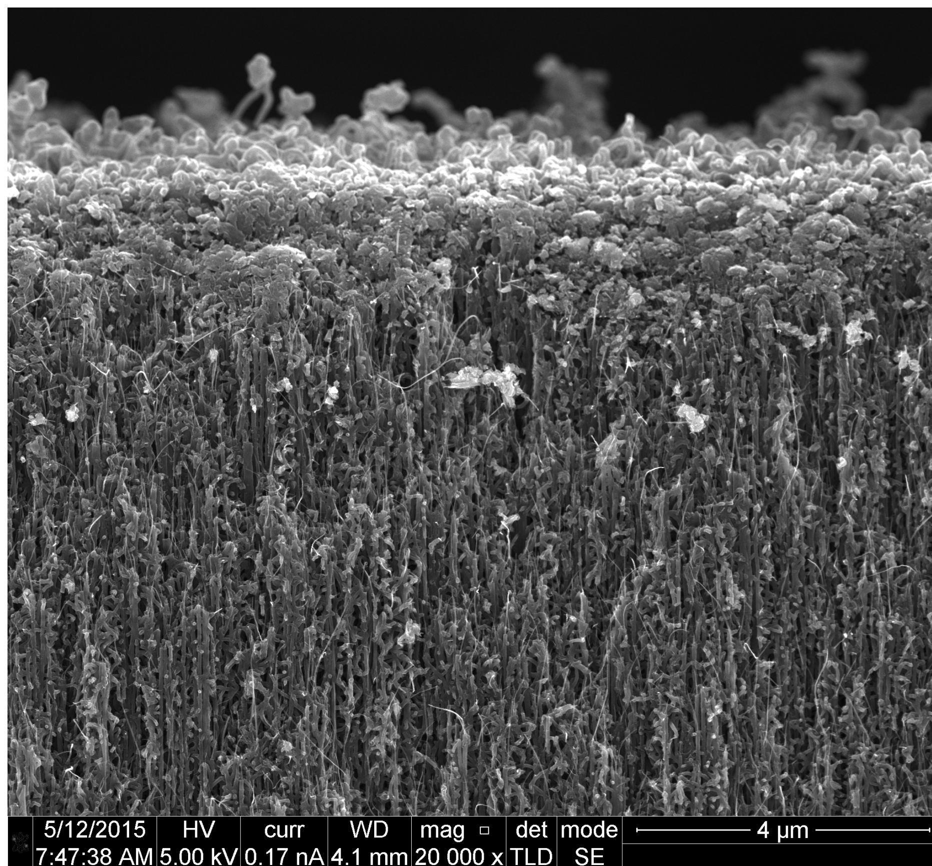

Figure 3.16 Visible capping at the top of a 5 minute infiltrated device.

massed again and then scraped from the substrate, which was itself massed. The percent mass remaining after the oxidation is shown in the figure. The height of the grown nanotubes forests were also measured before and after the oxidation, with the percent height remaining following a nearly identical trend as the mass remaining. This suggests that most of the mass removal occurs on the outside of the forest, which is beneficial if the desire is to remove external carbon and allow gas diffusion into the porous center of a cantilever sensor.

Additional confirmation that oxidation occurs more rapidly near the edges of CNT features can be found in Figure 3.18 where we see square nanotube forest features receeding from the edges more and more at higher temperatures. Note that each image represents a different sample, but that each was originally fabricated on the same chip and cleaved and oxidized separately afterward.

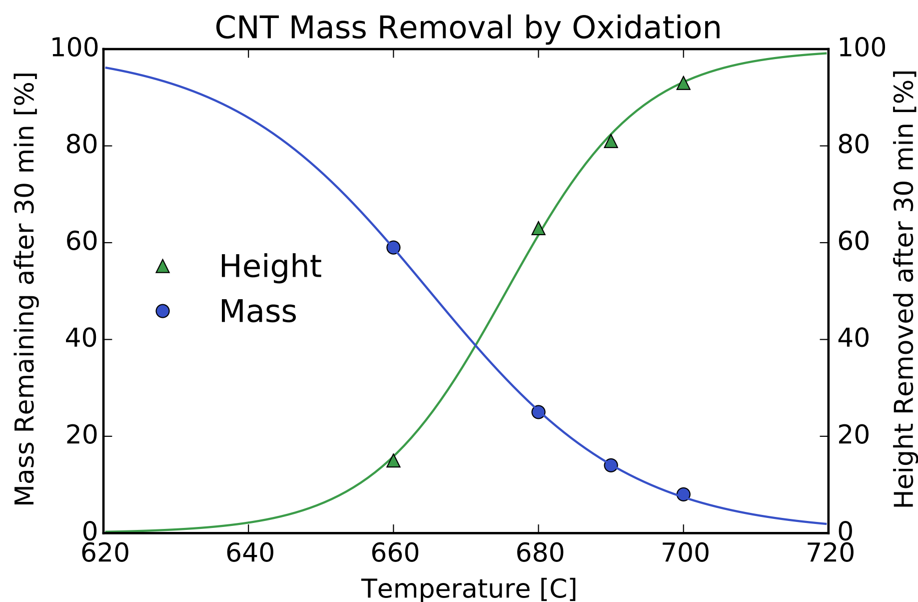

Figure 3.17 Data and models showing the percent of carbon nanotube mass and height removed after 30 minutes of oxidation at various temperatures. The models acompanying the data are fitted logistic curve models.

Note that the samples shown in Figure 3.18 were treated in the same way as the samples that were measured to create Figure 3.17.

These results indicate that possible challenges with cantilever device capping could be overcome by water vapor oxidation after the growth and infiltration steps.

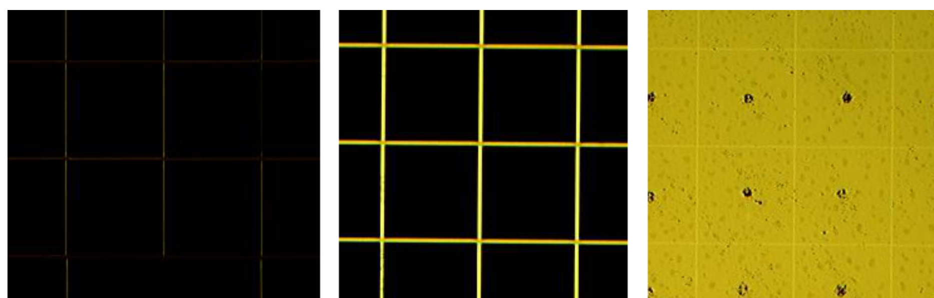

Figure 3.18 Images of oxidized carbon nanotube forests. Each sample was exposed to water vapor in hydrogen carrier gas for 30 minutes at 600 C, 650 C, and 800 C for the images from left to right.

3.5 Carbon Nanotube Morphology

The carbon nanotubes, before and after being coated, are generally not straight. Figure 3.19 shows that nanotubes near the base of a structure twist a great deal and are far from straight.

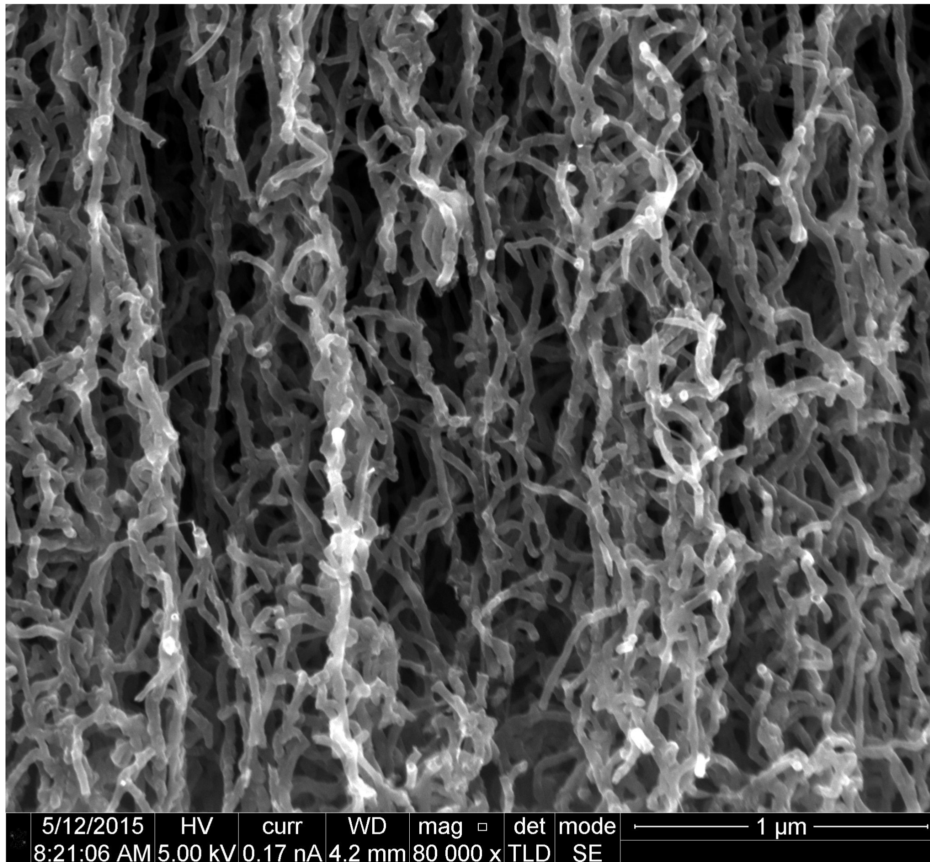

Figure 3.19 The bottom (near the iron catalyst) of a broken open 5 minute infiltrated device showing mostly twisting and non-parallel nanotube morphology.

Figure 3.20, however, shows that in the middle of a structure the coated carbon nanotubes are mostly straight and parallel.

When carbon is used as the infiltration material, the resulting composite material is observed to be highly compliant. The elastic modulus of the composite is typically between 1 and 5 GPa, varying with infiltration time.

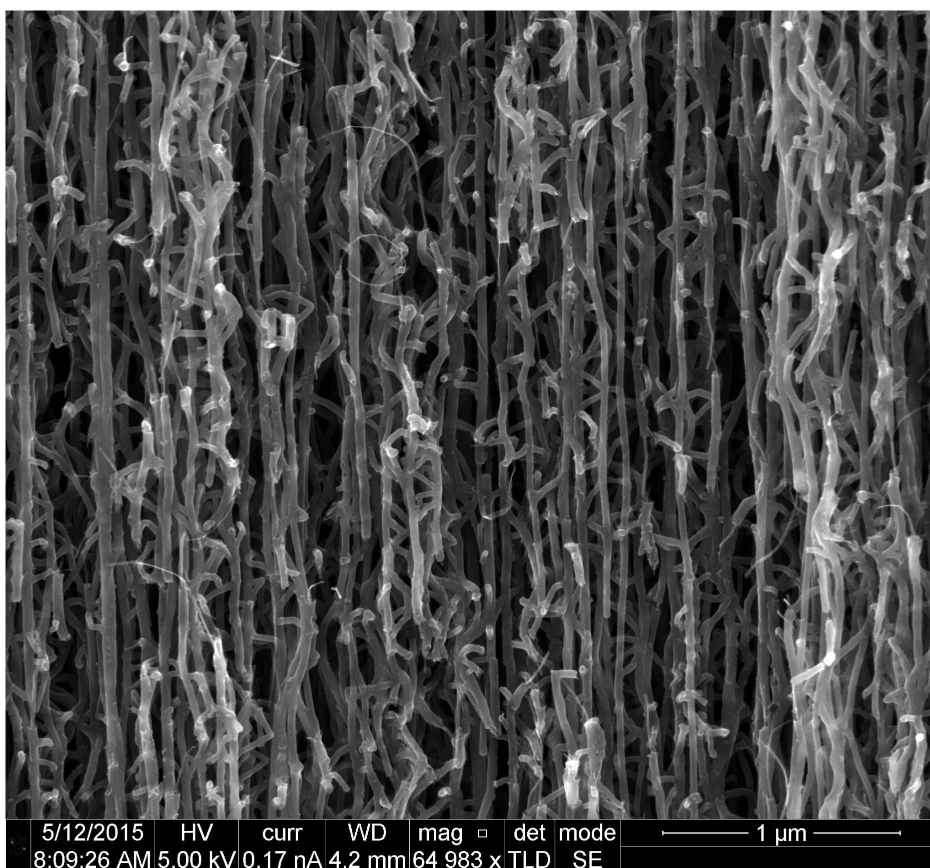

Figure 3.20 The center of a broken open 5 minute infiltrated device showing largely parallel and straight nanotube morphology.

Chapter 4

Cantilever Resonance Modeling

4.1 Introduction

The word "cantilever" is another name for a fixed-free beam, or any bar-like shape that is clamped at one end and free to move at the other end. In physics and engineering, countless structures are frequently treated as cantilevers, such as a golf club, a flag pole, a computer monitor, and a diving board. In addition, the same equation that describes a cantilever is equally valid for any beam (and is actually easier to solve). This means that the equation and solution presented below is also valid when solving systems such as I-beams in buildings, bridges, or any other odd shaped thing that is a few times longer in one direction than the others.

We are used to treating all sorts of things as springs and using Hooke's Law. That works great for things that are pushed or pulled along the direction of their length, but what about when they are pushed or pulled in a direction perpendicular to their length? This is where the beam equations come in. When solved in all their gory detail, they can be complicated, but the solutions provide simpler relationships that can be used more like Hooke's Law.

The beam equations can be solved for any arbitrary shape (although their validity requires that

one dimension be longer than the other two), but in order to simplify the already complicated derivations, we will look only at rectangular beams. Cylindrical beams, triangular beams, and others are not too hard to solve, but arbitrary shapes get complicated quickly.

In the sections below, we will first run through treating a cantilever as a Simple Harmonic Oscillator, just as a review to provide some insight and useful identities before we dive into the beam equation. We will also introduce a few new terms along the way.

4.2 Treating a Cantilever as a Simple Harmonic Oscillator

Because a cantilever is essentially a spring being pushed perpendicular to its length, Hooke's Law does not properly apply. If we apply it anyway, however, we begin with the following:

The force F is proportional to the displacement by the spring constant k, and we are going to add some damping to the model (air resistance, thermo-elastic dampening, etc.) with a coefficient c. We are also going to drive the oscillation with a sinusoidal driving force of angular frequency ω. Then,

$$F = -kx - cx' + \sin[\omega t]$$

or in other words,

$$mx'' = -kx - cx' + \sin[\omega t]$$

$$mx'' + cx' + kx = \sin[\omega t]$$

$$x'' + \frac{c}{m}x' + \frac{k}{m}x = \frac{1}{m}\sin[\omega t]$$

If we would have solved this equation with no damping and no driving force, we would have found that the natural frequency of vibration is $\omega_0 = \sqrt{\frac{k}{m}}$. Since this is a useful quantity to think about, let's substitute it in:

$$x'' + \frac{c}{\sqrt{mk}}\omega_0\, x' + \omega_0^2\, x = \frac{1}{m}\sin[\omega t]$$

This looks great, but we don't know much about that damping coefficient, c. A more common measurement in many fields is the Quality Factor, Q, which is defined to be

$$Q = 2\pi\,\frac{\text{Energy Stored in the Oscillations}}{\text{Energy Lost per Cycle}}$$

The quality factor is generally considered to be a property of the oscillator, similar to the natural frequency. To give a couple examples, a tuning fork has a very high quality factor, while a regular fork does not. Resonators with high quality factors take a long time to "ring down," or stop resonating. They also only respond to a narrow range of frequencies (they have a sharp resonance peak), while low Q oscillators will respond to many frequencies (they have a broad resonance peak). We will use Q for many reasons, but one of them is that it turns out that

$$Q = \frac{\sqrt{mk}}{c}$$

This means that we can easily substitute Q in for c in our differential equation to obtain:

$$x'' + \frac{1}{Q}\omega_0\, x' + \omega_0^2\, x = \frac{1}{m}\sin[\omega t]$$

The solution to this equation has two parts, the transient part and the steady state part. Since the transient part dies away quickly, the part that we are most interested in is the steady state part. Upon solving, the steady state solution to this equation is:

$$\frac{\left(\omega_0^2-\omega^2\right)}{m\left(\frac{1}{Q^2}\omega^2\omega_0^2+\left(\omega_0^2-\omega^2\right)\right)}\sin[\omega t] - \frac{\omega\omega_0}{mQ\left(\frac{1}{Q^2}\omega^2\omega_0^2+\left(\omega_0^2-\omega^2\right)\right)}\cos[\omega t]$$

This is written out as a sum of a sine and a cosine, but the origin of time zero is arbitrary, so all we can measure in a steady state oscillation is the amplitude and the phase. We can think of

this as translating the above function into the form $A\cos[\omega t+\phi]$, where A is the amplitude and ϕ is the phase shift. For the amplitude, we simply need to use the pathagorean theorem, such that the amplitude is:

$$A=\sqrt{\left(\frac{(-\omega^2+\omega_0^2)}{m\left(\frac{1}{Q^2}\omega^2\omega_0^2+\left(-\omega^2+\omega_0^2\right)^2\right)}\right)^2+\left(\frac{-\omega\omega_0}{mQ\left(\frac{1}{Q^2}\omega^2\omega_0^2+\left(-\omega^2+\omega_0^2\right)^2\right)}\right)^2}$$

Upon simplification, we have:

$$A=\frac{1}{m\sqrt{\left(\frac{\omega\omega_0}{Q}\right)^2+\left(\omega_0^2-\omega^2\right)^2}}$$

Next, to find the difference in phase between the drive and the response, we need to take the arctangent of the ratio of the amplitude of the cosine to the amplitude of the sine, as follows:

$$\phi=\arctan\left(\left(\frac{-\omega\omega_0}{mQ\left(\frac{1}{Q^2}\omega^2\omega_0^2+\left(-\omega^2+\omega_0^2\right)^2\right)}\right)/\left(\frac{(-\omega^2+\omega_0^2)}{m\left(\frac{1}{Q^2}\omega^2\omega_0^2+\left(-\omega^2+\omega_0^2\right)^2\right)}\right)\right)$$

Upon simplification, we have:

$$\phi=\arctan\left(\frac{\omega\omega_0}{Q\left(\omega^2-\omega_0^2\right)}\right)$$

These are the desired results. In order to understand them, it is helpful to look at some plots. For the following plots, the resonant frequency will be set to 5 cycles per second, and the mass to 2 kg.

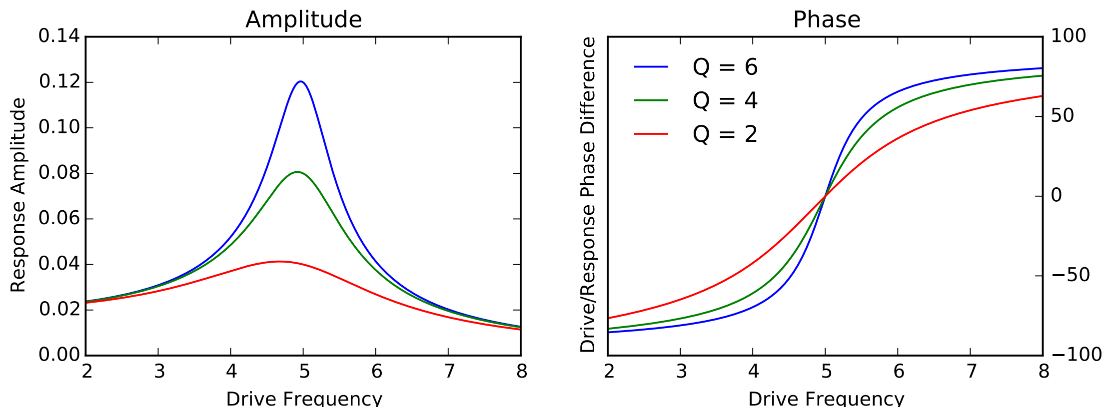

Figure 4.1 Example plots of the simple harmonic oscillator solution showing the effect of quality factor on the behavoir.

4.3 Fitting Cantilever Resonance Data

Although it is true that the Simple Harmonic Oscillator equation does not entirely describe a cantilever, it does provide the functional forms of the amplitude versus frequency and phase shift versus frequency. Thus, although we will go on to solve the cantilever equations in order to learn a great deal about how cantilevers vibrate and what their resonant frequencies will be and such, we have already covered enough ground that we can discuss fitting cantilever resonance data. Fitting is useful in this case because it allows for a much better estimation of the resonance frequency than simply measuring the frequency at which the response is a maximum, and also because fitting is the most reliable method of determining the Quality Factor of a cantilever (an estimation can be obtained by measuring the resonance peak's full width at half maximum and dividing by the resonant frequency).

4.4 Cantilever Equation Solution

To predict a cantilevers resonant frequency and other characteristics, it is required to solve the beam equation for a cantilever rather than simply the harmonic oscillator equation. The partial differ-

ential equation describing a cantilever under the assumption of small deflections and no damping is

$$\frac{EWH^3}{12}u_{\mathrm{xxxx}} = -WH\rho u_{\mathrm{tt}}$$

We will now proceed to describe and solve this equation.

4.4.1 Definition of Variables

Let the function $u(x,t)$ be the deflection of the cantilever section at position x and time t, where the cantilever is clamped at position $x = 0$ and free at the position $x = L$ (where L represents the length of the cantilever). Also let subscripts represent partial derivatives in the variable subscripted, and constants be defined as follows:

- E - The Youngs Modulus of the cantilever material
- W - The width of the cantilever
- H - The height of the cantilever, or thickness in the direction of vibration
- L - The length of the cantilever
- ρ - The density of the cantilever material
- c - A damping coefficient, likely a function of other variables, that will be explored later

For simplicity, let a constant β be defined as

$$\beta = \left(\frac{12}{EWH^3}\right)^{\frac{1}{4}}$$

4.4.2 The Boundary Conditions

- $u(0,t) = 0$

- $u_x(0,t) = 0$
- $u_{\mathrm{xx}}(L,t) = 0$
- $u_{\mathrm{xxx}}(L,t) = 0$

4.4.3 Separation of Variables

Let $u(x,t) = f(x)g(t)$, then

$$\frac{EWH^3}{12}\frac{f''''(x)}{f(x)} = -WH\rho\frac{g''(t)}{g(t)} = \alpha^4$$

4.4.4 The Time Equation

$$WH\rho g''(t) = -\alpha^4 g(t)$$

and so

$$g(t) = C_1 \cos\left(\frac{\alpha^2}{\sqrt{WH\rho}}t\right) + C_2 \sin\left(\frac{\alpha^2}{\sqrt{WH\rho}}t\right)$$

4.4.5 The Spacial Equation

$$f''''(x) = \frac{12\alpha^4}{EWH^3}f(x)$$

or

$$f''''(x) = \alpha^4\beta^4 f(x)$$

and so

$$f(x) = C_3\cos[\beta\alpha x] + C_4\sin[\beta\alpha x] + C_5E^{\beta\alpha x} + C_6E^{-\beta\alpha x}$$

or

$$f(x) = C_3(\cos[\beta\alpha x] + \cosh[\beta\alpha x]) + C_4(\cos[\beta\alpha x] - \cosh[\beta\alpha x]) \\ + C_5(\sin[\beta\alpha x] + \sinh[\beta\alpha x]) + C_6(\sin[\beta\alpha x] - \sinh[\beta\alpha x])$$

4.4.6 Applying Boundary Conditions

Since $u(0,t) = 0$ we know that $f(0) = 0$ and thus $C_3 = 0$. Also, since $u_x(0,t) = 0$ we know that $f'(0) = 0$ and thus $C_5 = 0$. As a result,

$$f(x) = C_4(\cos[\alpha\beta x] - \cosh[\alpha\beta x]) + C_6(\sin[\alpha\beta x] - \sinh[\alpha\beta x])$$

$$f''(x) = C_4\left(-\alpha^2\beta^2\cos[\alpha\beta x] - \alpha^2\beta^2\cosh[\alpha\beta x]\right) + C_6\left(-\alpha^2\beta^2\sin[\alpha\beta x] - \alpha^2\beta^2\sinh[\alpha\beta x]\right)$$

$$f'''(x) = C_6\left(-\alpha^3\beta^3\cos[\alpha\beta x] - \alpha^3\beta^3\cosh[\alpha\beta x]\right) + C_4\left(\alpha^3\beta^3\sin[\alpha\beta x] - \alpha^3\beta^3\sinh[\alpha\beta x]\right)$$

Thus, since $u_{\text{xx}}(L,t) = 0, f''(L) = 0$, we have

$$C_4\left(-\alpha^2\beta^2\cos[\alpha\beta L] - \alpha^2\beta^2\cosh[\alpha\beta L]\right) + C_6\left(-\alpha^2\beta^2\sin[\alpha\beta L] - \alpha^2\beta^2\sinh[\alpha\beta L]\right) = 0$$

As a result,

$$C_6 = C_4\frac{-\cos[\alpha\beta L] - \cosh[\alpha\beta L]}{\sin[\alpha\beta L] + \sinh[\alpha\beta L]}$$

Such that

$$f(x) = C_4 \left((\cos[\alpha\beta x] - \cosh[\alpha\beta x]) + \frac{-\cos[\alpha\beta L] - \cosh[\alpha\beta L]}{\sin[\alpha\beta L] + \sinh[\alpha\beta L]} (\sin[\alpha\beta x] - \sinh[\alpha\beta x]) \right)$$

Also, since $u_{\text{xxx}}(L,t) = 0$, we must have $f'''(L) = 0$, or

$$C_4 \frac{-\cos[\alpha\beta L] - \cosh[\alpha\beta L]}{\sin[\alpha\beta L] + \sinh[\alpha\beta L]} \left(-\alpha^3\beta^3 \cos[\alpha\beta L] - \alpha^3\beta^3 \cosh[\alpha\beta L]\right)$$
$$+ C_4 \left(\alpha^3\beta^3 \sin[\alpha\beta L] - \alpha^3\beta^3 \sinh[\alpha\beta L]\right) = 0$$

Which simplifies to

$$\frac{1 + \cos[L\alpha\beta] \cosh[L\alpha\beta]}{\sin[L\alpha\beta] + \sinh[L\alpha\beta]} = 0$$

or

$$1 + \cos[L\alpha\beta] \cosh[L\alpha\beta] = 0$$

This means that α cannot take on any value, but only certain discrete values, the nth of which we will call α_n

To simplify our discussion, let us define a new variable, k_n, such that $k_n = \alpha_n \beta L$. For clarity, this means that α_n is now given by $\alpha_n = \frac{k_n}{\beta L}$.

Re-writing the equation above with this new variable, we have

$$1 + \cos(k_n) \cosh(k_n) = 0$$

The possible values of k_n are given by the roots of the above transcendental equation. The first 10 of these values are:

Since the hyperbolic cosine function grows rapidly, it can be seen that these solutions are nearly given by

k_n	Value
k_0	1.875104068711961
k_1	4.694091132974175
k_2	7.854757438237613
k_3	10.99554073487547
k_4	14.13716839104647
k_5	17.27875953208824
k_6	20.42035225104125
k_7	23.56194490180644
k_8	26.7035375555183
k_9	29.84513020910282

Table 4.1 The first ten constants governing cantilever bending behavior

$$\cos(k_n) = \frac{-1}{\cosh(k_n)} \approx 0$$

which means that

$$k_n \approx \left(n + \frac{1}{2}\right)\pi, \quad n \in Z$$

This approximation is not accurate for the first possible value $(n = 0)$, but quickly becomes extremely accurate as n increases.

4.4.7 Substituting for the Separation Constant

Since $\alpha_n = \frac{k_n}{\beta L}$, and $\beta = \left(\frac{12}{EWH^3}\right)^{\frac{1}{4}}$, we can now substitute into the previously found equations

$$f(x) = C_4\left((\cos[\alpha\beta x] - \cosh[\alpha\beta x]) + \frac{-\cos[\alpha\beta L] - \cosh[\alpha\beta L]}{\sin[\alpha\beta L] + \sinh[\alpha\beta L]}(\sin[\alpha\beta x] - \sinh[\alpha\beta x])\right)$$

$$g(t) = C_1 \cos\left(\frac{\alpha^2}{\sqrt{WH\rho}} t\right) + C_2 \sin\left(\frac{\alpha^2}{\sqrt{WH\rho}} t\right)$$

To obtain

$$f(x) = C_4 \left(\left(\cos\left(\frac{k_n x}{L}\right) - \cosh\left(\frac{k_n x}{L}\right) \right) + \frac{-\cos(k_n) - \cosh(k_n)}{\sin(k_n) + \sinh(k_n)} \left(\sin\left(\frac{k_n x}{L}\right) - \sinh\left(\frac{k_n x}{L}\right) \right) \right)$$

$$g(t) = C_1 \cos\left(k_n^2 \frac{H}{L^2} \sqrt{\frac{E}{12\rho}} t\right) + C_2 \sin\left(k_n^2 \frac{H}{L^2} \sqrt{\frac{E}{12\rho}} t\right)$$

4.4.8 The Final Solution

As a result of the above derivations, it can be seen that

$$u(x,t) = \sum_{n=1}^{\infty} f(x) g(t)$$

Therefore, after combining constants and replacing them with counterparts that have different values for different values of n (which we call A_n and B_n), we obtain for the final solution

$$u(x,t) = \sum_{n=1}^{\infty} \left(\left(\cos\left(\frac{k_n x}{L}\right) - \cosh\left(\frac{k_n x}{L}\right) \right) + \frac{-\cos(k_n) - \cosh(k_n)}{\sin(k_n) + \sinh(k_n)} \left(\sin\left(\frac{k_n x}{L}\right) - \sinh\left(\frac{k_n x}{L}\right) \right) \right) \left(A_n \cos\left(k_n^2 \frac{H}{L^2} \sqrt{\frac{E}{12\rho}} t\right) + B_n \sin\left(k_n^2 \frac{H}{L^2} \sqrt{\frac{E}{12\rho}} t\right) \right)$$

Where A_n and B_n may be determined from the initial shape of the beam.

4.4.9 The Resonant Frequency

The natural frequency of the cantilever is then

$$\omega_0 = k_n^2 \frac{H}{L^2} \sqrt{\frac{E}{12\rho}}$$

$$f_0 = \frac{k_n^2}{2\pi} \frac{H}{L^2} \sqrt{\frac{E}{12\rho}}$$

4.4.10 Resonant Modes

Since the natural frequencies of the beam depend on k_n^2, it is informative to give a table of the values of k_n^2, and also to give a table of the values of k_n^2/k_1^2. Such a table is provided in Table 4.2.

This means that the first "harmonic" of a cantilever has ∼6.3 times the frequency of the fundamental, the second "harmonic" ∼ 17.5 times the frequency of the fundamental, etc. This is clearly different than many other systems such as instrument strings and similar. In fact, these other modes are not harmonics, but simply other resonant modes. Due to the fixed-free boundary conditions of a cantilever, the frequencies are not integer multiples, but conceptually the modes are similar to a harmonic series.

k_n^2	k_n^2/k_1^2
3.516015268500151	1.
22.03449156466677	6.266893025770666
61.69721441354911	17.54748193680845
120.9019160523057	34.38606115720301
199.8595301168034	56.84262292810201
298.5555309677301	84.9130359707132
416.9907860566054	118.5975469994144
555.1652475557627	157.8961424114017
713.0789179789761	202.8088229216248
890.731797198302	253.3355884936946
1088.123885220102	309.4764391294211
1305.255182044067	371.2313748287158
1542.125687670212	438.6003955915831
1798.735402098535	511.5835014180225
2075.084325329038	590.1806923080342
2371.172457361719	674.3919682616182
2686.999798196578	764.2173292787744
3022.566347833616	859.656775359503
3377.872106272833	960.710306503804
3752.917073514229	1067.377922711676
4147.701249557803	1179.659623983122

Table 4.2 Cantilever mode frequency constants

4.5 Adding a Linear Damping Term

The above solution is extremely useful, but for some applications more information is needed. For example, the above solution did not consider the effect of damping. Below are the differences in solution when a linear damping term is added to the equation. The differential equation now becomes

$$\frac{EWH^3}{12}u_{\mathrm{xxxx}} = -WH\rho u_{\mathrm{tt}} - cu_t$$

This leads to a time equation of

$$g(t) = e^{\frac{-ct}{2HW\rho}}\left(C_1\cos\left(\frac{t\sqrt{4HW\alpha^4\rho - c^2}}{2HW\rho}\right) + C_2\sin\left(\frac{t\sqrt{4HW\alpha^4\rho - c^2}}{2HW\rho}\right)\right)$$

while the spacial equation remains the same.

The final solution is then:

$$u(x,t) = \sum_{n=1}^{\infty}\left(\left(\cos\left(\frac{k_n x}{L}\right) - \cosh\left(\frac{k_n x}{L}\right)\right) + \frac{-\cos(k_n) - \cosh(k_n)}{\sin(k_n) + \sinh(k_n)}\left(\sin\left(\frac{k_n x}{L}\right) - \sinh\left(\frac{k_n x}{L}\right)\right)\right)$$
$$\left(A_n\cos\left(\frac{t\sqrt{EH^4W^2\rho k_n^4 - 3L^4c^2}}{\sqrt{12}L^2HW\rho}\right) + B_n\sin\left(\frac{t\sqrt{EH^4W^2\rho k_n^4 - 3L^4c^2}}{\sqrt{12}L^2HW\rho}\right)\right)e^{\frac{-ct}{2HW\rho}}$$

4.5.1 The Resonant Frequency

The natural frequencies of the cantilever are then:

$$\omega_0 = \frac{\sqrt{EH^4W^2\rho k_n^4 - 3L^4c^2}}{\sqrt{12}L^2HW\rho}$$

$$f_0 = \frac{\sqrt{EH^4W^2\rho k_n^4 - 3L^4c^2}}{2\pi\sqrt{12}L^2HW\rho}$$

4.5.2 The Effect of Damping with Respect to Geometry

When damping is included in the model, it effects the resonant frequency differently for different changes in the geometry of the cantilever.

4.5.3 Relating the Damping Coefficient to the Quality factor

From the decay rate, we can see that

$$c = \frac{2\pi f_0 H W \rho}{Q}$$

As an approximation, we can estimate this as

$$c \approx \frac{W}{Q}\left(k_n \frac{H}{L}\right)^2 \sqrt{\frac{E\rho}{12}}$$

Apart from the approximation, we can exacly write the resonance frequency as

$$f_n = \frac{k_n^2}{2\pi}\frac{H}{L^2}\frac{Q}{\sqrt{3+12Q^2}}\sqrt{\frac{E}{\rho}}$$

This is the damped resonant frequency of a cantilever experiencing linear fluid damping. This frequency depends on the quality factor of the system, which is determined both by properties of the beam itself and the nature of the fluid damping. As expected, this frequency is always less than the undamped resonant frequency, approaching that limit as the quality factor tends to infinity.

4.6 Adding a Drive Term

In order to solve for the spectrum as we did with the harmonic oscillator model, we need to include a drive term. The equation to solve in this case is then

$$\frac{EWH^3}{12}u_{\mathrm{xxxx}} = -WH\rho u_{\mathrm{tt}} - cu_t + a\sin(\omega t)$$

4.7 Nonlinearities

All above solutions have assumed that deflections are small. When deflections are larger, cantilevers experience what is called the geometric nonlinearity, which causes the resonance peak to shift and begin to roll over, like the classic illustration of an ocean wave. This nonlinearity is described by the following equation.

$$\frac{EWH^3}{12}u_{\mathrm{xxxx}} - \frac{3}{2}EWHu_{\mathrm{xx}}u_x^2 = -WH\rho u_{\mathrm{tt}} - cu_t$$

4.8 Quadratic Drag

In most environments a microcantilever is exposed to, the Reynolds number of the fluid flow around the cantilever is small. When this is the case, the above linear drag model is sufficient. If, however, the Reynold's number becomes larger (than about 1000), it may become necessary to add a quadratic drag term and solve the equation

$$\frac{EWH^3}{12}u_{\mathrm{xxxx}} = -WH\rho u_{\mathrm{tt}} - cu_t^2$$

4.9 Timoshenko Beam Theory

All of the above PDEs come from what is called Euler Bernoulli Beam Theory. This theory is powerful and widely used, but it assumes that the material of the beam cannot deform in shear and

also ignores rotational inertial effects. A much better model of beam motion is the Timoshenko Beam Theory. The primary equation that this theory provides is

$$\frac{EWH^3}{12}u_{\mathrm{xxxx}} - \left(\frac{\rho WH^3}{12} + \frac{E\rho WH^3}{12\kappa G}\right)u_{\mathrm{xxtt}} = -\frac{WH^3\rho^2}{12\kappa G}u_{\mathrm{tttt}} - WH\rho u_{\mathrm{tt}}$$

Where

- G - The Material Shear Modulus
- κ - The Timoshenko Shear Coefficient, geometrically determined, normally $\frac{5}{6}$

For a beam with rectangular cross section,

$$\kappa \approx \frac{6(1+\nu)}{7+6\nu}$$

with ν being the Poisson's Ratio of the material.

4.10 Cantilever Relations

4.10.1 Stress-Displacement Relations

In the following equations,

- δ is the displacement of the end of the cantilever
- σ is the applied stress
- F is the applied force
- ε is the strain
- ν is the Poisson's ratio of the cantilever material (about .2)

and the other variables are as defined previously.

Basic Relation

$$\delta = \frac{3\sigma(1-\nu)}{E}\frac{L^2}{H}$$

$$\sigma = \frac{6L}{WH^2}F$$

$$\varepsilon = \frac{E}{\sigma}$$

Derived Relations

For quick reference, the above equations can be arranged into the following forms:

$$\delta = \frac{18(1-\nu)}{EW}\left(\frac{L}{H}\right)^3 F$$

$$\sigma = \frac{E}{3(1-\nu)}\frac{H}{L^2}\delta$$

$$F = \frac{WH^2}{6L}\sigma$$

$$F = \frac{EW}{18(1-\nu)}\left(\frac{H}{L}\right)^3 \delta$$

Chapter 5

Resonance Testing

5.1 Cantilever Mount and Drive

In preparation for resonance testing, a device was placed on the tip of a piezoelectric bimorph, with the base of the cantilever lining up with the top edge of the piezoelectric. This stack was then clamped between two stainless steal plates, with the top edge of the plates also aligned to the top of the piezoelectric as shown in Figure 5.1.

The piezoelectric was used to drive the cantilever into resonance. A sinusoidal voltage signal applied to the piezo causes it to oscillate, providing mechanical energy to the system at the frequency of the sinusoid. The portion of this energy the cantilever received and retained was frequency dependant. When the piezoelectric drove energy into the system at a frequency near a resonant mode frequency of the cantilever, the cantilever oscillation amplitude was increased. At other frequencies, the cantilever did not oscillate appreciably.

The effect of changing the power of the driving force from the piezoelectric on the response of the cantilver can be seen in Figure 5.2. Note that the measured resonant frequency of the cantilever does shift with applied voltage to the piezoelectric.

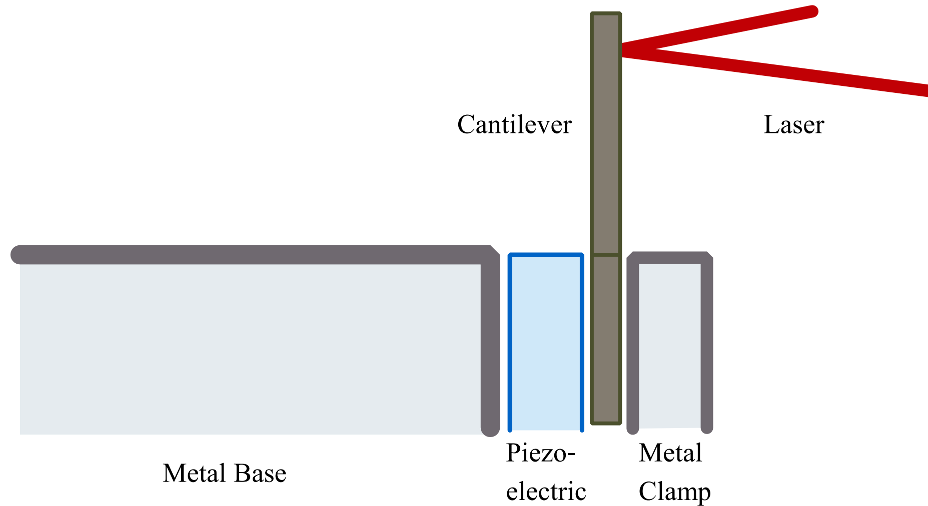

Figure 5.1 A cantilever is mounted by clamping it directly between a stainless steel plate and a piezo-electric bimorph. The top of the clamp, the top of the piezo-electric, and the bottom of the cantilever are all aligned. During resonance testing, a laser is reflected from the tip of the cantilever to be measured by a photodiode.

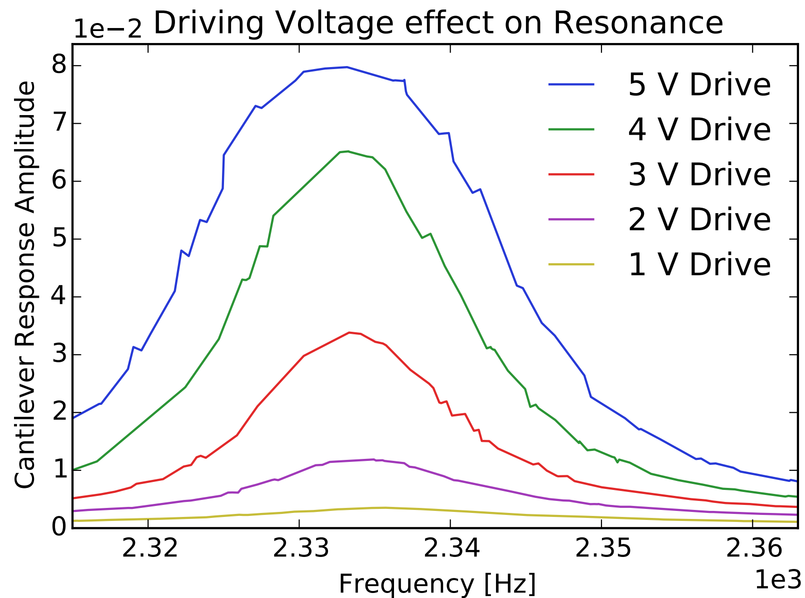

Figure 5.2 Effect of driving voltage on resonance peaks

Figure 5.3 shows that the cantilever tip deflection angle varies linearly with the applied voltage to the piezoelectric.

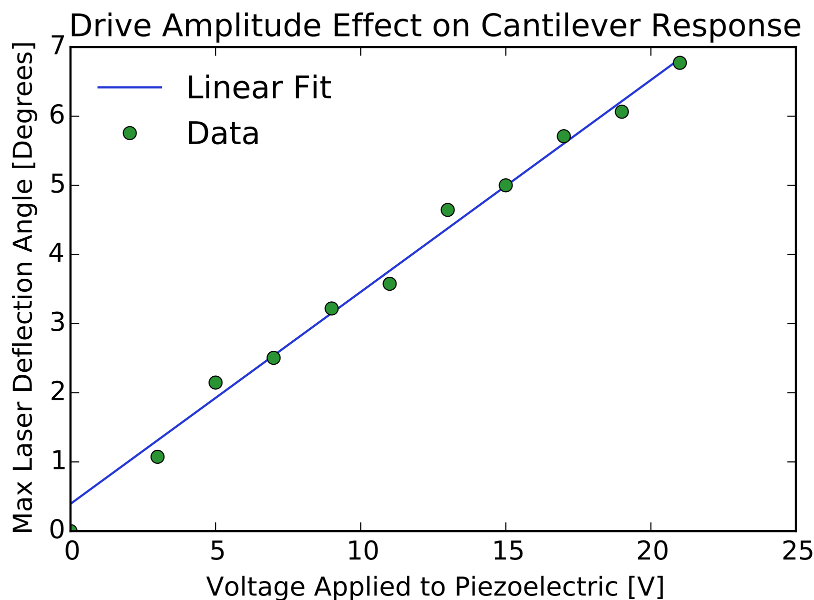

Figure 5.3 Effect of drive voltage on cantilever tip deflection

5.2 Cantilever Measurement

A laser was reflected from the tip of the device to a photodiode for measurement. The tip of the reflected beam was centered on the photodiode, causing the total amount of light reaching the photodiode face to vary with the deflection of the cantilever.

A lock-in amplifier was used to provide a sinusoidal voltage to the piezoelectric at a controlled frequency, driving the cantilever into resonance. The same instrument was simultaneously used to measure the voltage across the photodiode. The amplifier was locked to its output. As a result, the lock-in amplifier produced the component of the photodiode response at the drive frequency.

The lock-in amplifier was computer controlled by means of LabVIEW software. This allowed for controlled frequency sweeps, precise timing, and data collection replication to promote statistical validity of the results obtained.

The resonant peak of a given cantilever can be scanned with high accuracy and tracked with fidelity. This can be seen to some degree in Figure 5.4, where 1000 resonance peak scans taken

over a period of approximately 10 hours are superimposed. The resonance and measurement are seen to be quite consistent over this time period. Additionaly, when these data sets are fitted and the actual resonant frequency observed over time, it becomes clear that the resonant frequency cycles with the same approximate period as a typical air conditioning system. Since these measurements were not taken in a controlled environment, it appears that much of the apparent noise in the data is not coming from the measurement, but is rather the result of a correct measurement of a cantilever experiencing a time variable environment.

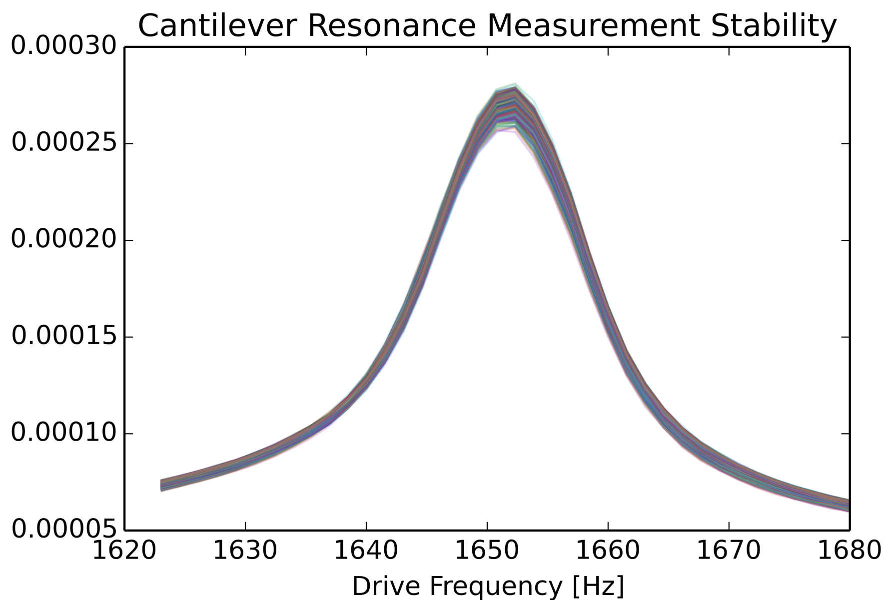

Figure 5.4 Shown are 1000 scans of the same resonance peak. It can be seen that the parameters of the peak can be measured reliably and accurately. The shifts in the peak are largely due to temperature variations in the room during the excess of 10 hours during which this data was taken.

A Lorentzian curve resulting from a simple harmonic oscillator model of the cantilevers was fit to each data set in order to compute resonance frequencies and quality factors. Although in some cases cantilever resonance peaks can deviate from the simple harmonic oscillator model, devices tested were found to be in good agreement with the model. An example of this agreement can be seen in Figure 5.5.

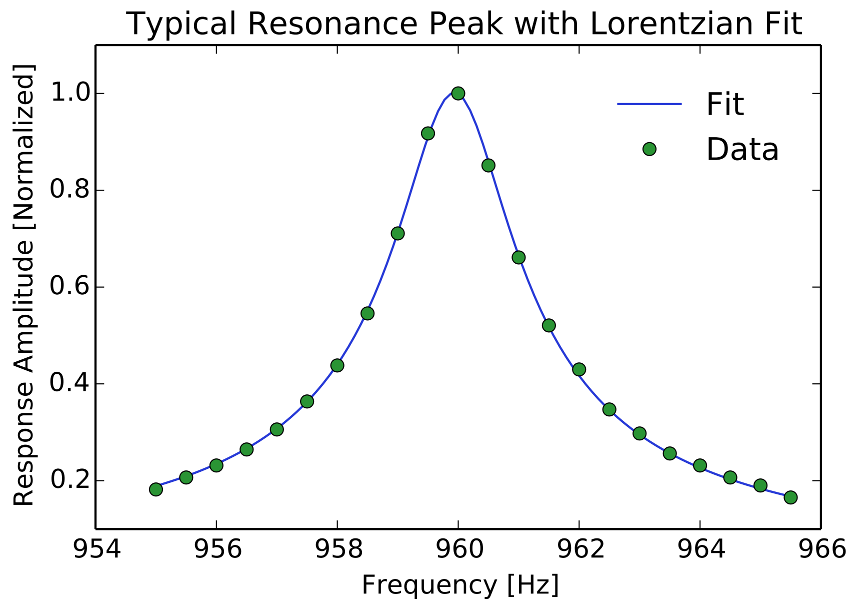

Figure 5.5 A set of resonance data ploted alongside a Lorentzian fit of the same. Details of the fitting function can be found in the text.

5.3 Nonlinearities

In some cases, however, behavior deviating from that of a simple harmonic oscillator was observed. For example, when cantilevers were driven to large amplitudes, nonlinear effects became apparent. These effects were modeled by numerically solving the cantilever partial differential equation with linear damping. Results of this modeling can be seen in Figure 5.6.

A corresponding measurement verifying the trends predicted by the model can be seen in Figure 5.7

These nonlinear effects can be used to glean more information about the cantilevers and their environments, such as by providing an additional method of measuring fluid damping.

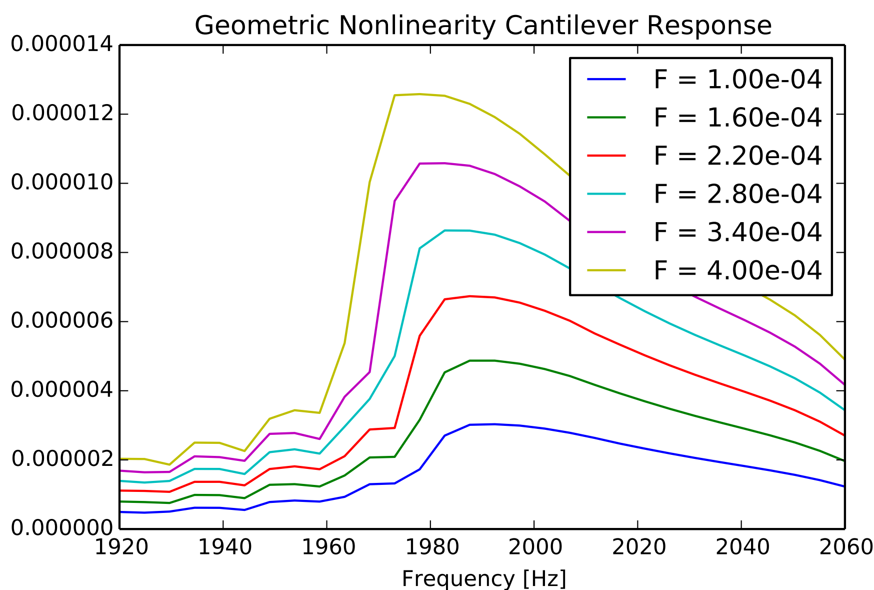

Figure 5.6 A series of simulated resonance peaks showing increasing nonlinear behavior for increasing drive amplitudes.

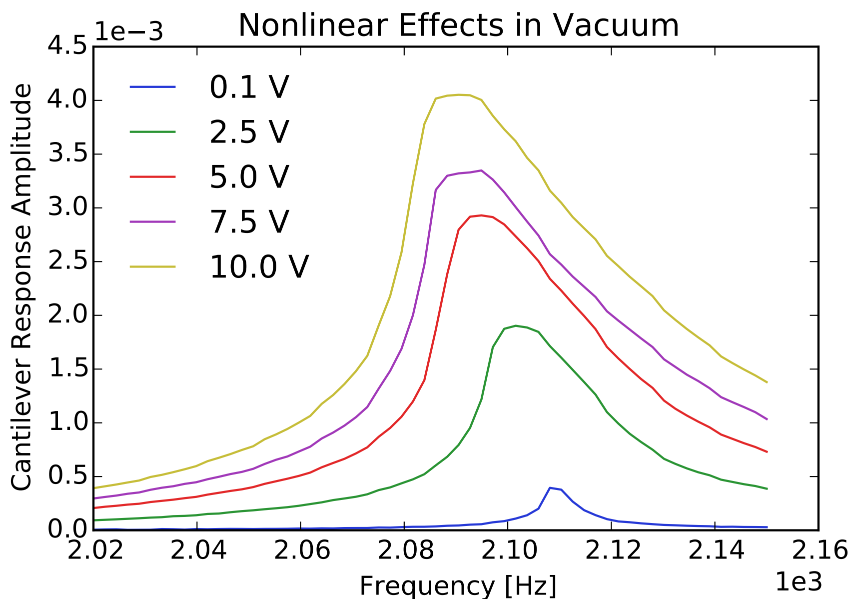

Figure 5.7 Actual cantilever resonance peaks taken at different drive amplitudes that show nonlinear behavior.

5.4 Multiple Resonant Modes

Although the fundamental resonant mode of the cantilevers was the most frequently studied, multiple modes were observed in some cases. Flexural modes in the direction of the cantilever height as well as in the direction of the width were seen, in addition to torsional beam modes. Figure 5.8 shows the frequency response of one cantilever, illustrating the first and second flexural modes of a cantilever in the direction of the height of the beam (the most frequent mode direction studied).

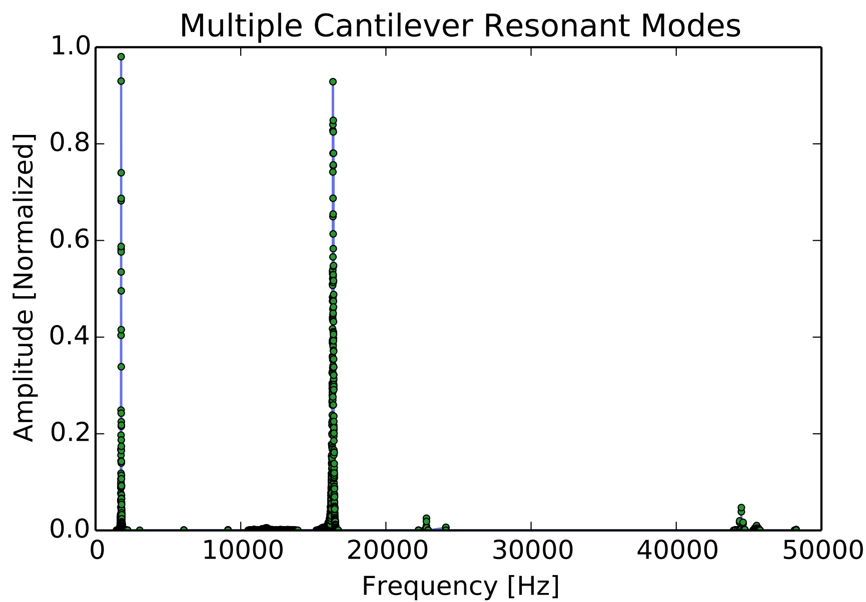

Figure 5.8 A frequency scan showing multiple resonance modes of a single cantilever.

5.5 Resonant Frequency dependance on Geometry

As expected, cantilever resonant frequencies were found to vary with beam geometry as predicted. An example of this can be seen in Figure 5.9

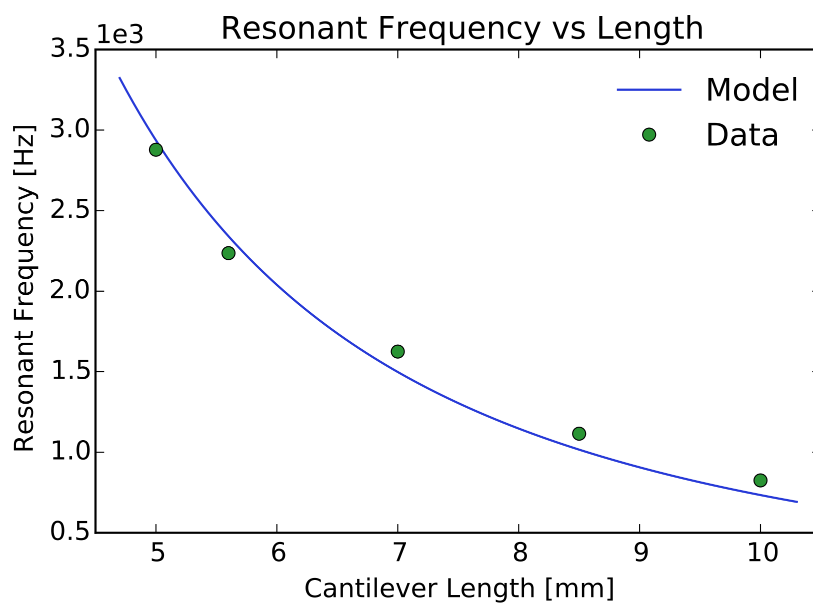

Figure 5.9 Length dependence of resonant frequency

Chapter 6

Fluid Drag

Because these porous cantilever sensors are meant to be used in fluid environments, understanding fluid drag on these beams becomes a major concern. Much can be determined by changing the pressure a cantilever is exposed to while it is resonating. Figure 6.1 shows how a resonance peak shifts and scales as pressure is varied.

Figure 6.2 shows how the damped resonant frequency of a beam changes with pressure. This frequency is expected to go down with increased pressure, as the beam effectively gains the mass of the air it drags with it or pushes out of its way.

Figure 6.3 shows the variation in quality factor with gas pressure. The quality factor goes down as pressure is increased because more energy is lost to the fluid.

Figure 6.4 shows the damping ratio as it changes with pressure. This ratio is related to the quality factor by $\zeta = 1/(2Q)$ but can be more convenient to discuss when discussing how different sources of damping add, because while damping ratios add and are a measure of damping from a source, quality factors are related by the sum of inverses being the inverse of the effective.

Figure 6.5 distinguishes between damping coming from fluid drag and that coming from other sources such as clamping loss or internal Thermo Elastic Dampening (TED).

We can see from Figure 6.5 that TED is certainly not dominant when pressures reach near

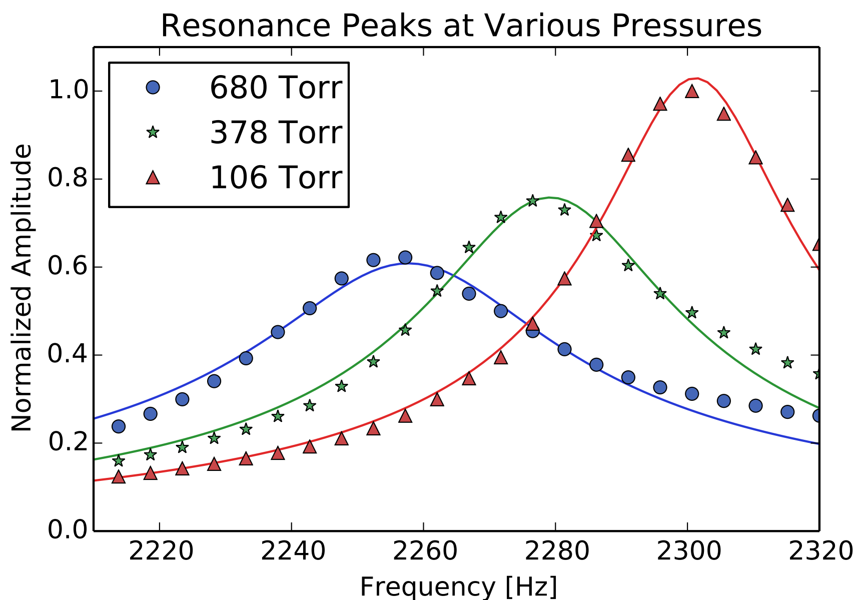

Figure 6.1 Resonance data of a single cantilever in a gas environment of three different pressures are shown alongside a model fitted to each case that was used to extract the resonance frequency and quality factor.

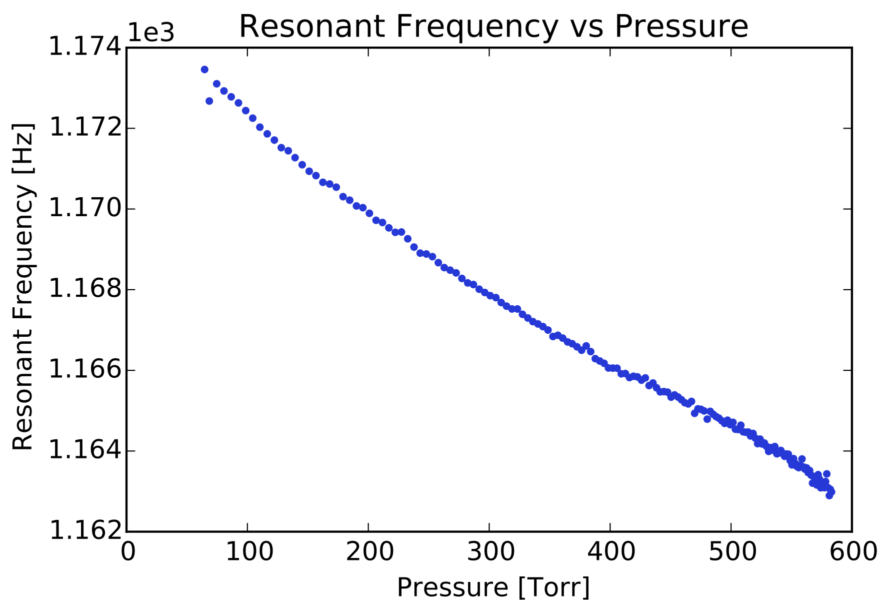

Figure 6.2 The resonant frequency of a given beam is shown as the beam is exposed to different gas pressures.

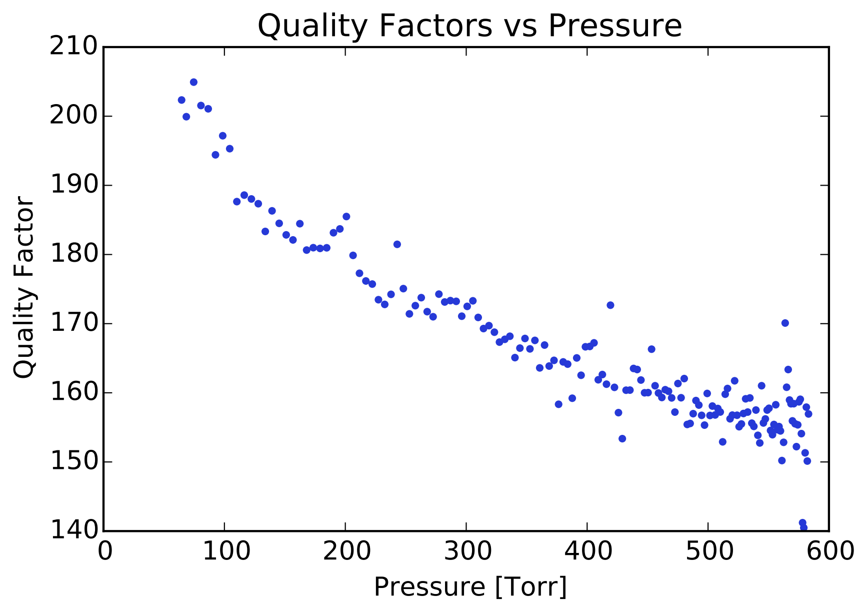

Figure 6.3 The quality factor of a given beam is shown as the beam is exposed to different gas pressures.

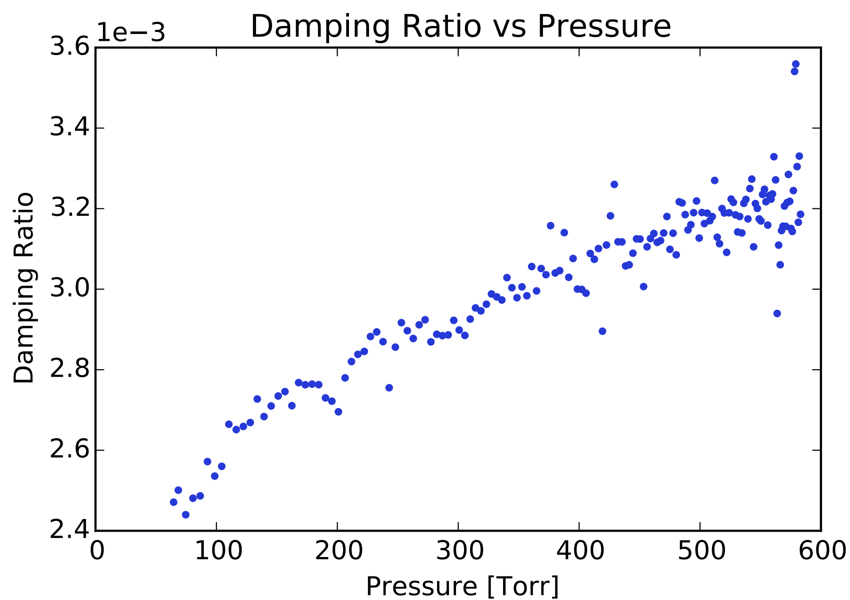

Figure 6.4 The value of the damping ratio ($\zeta = 1/(2Q)$) for a given cantilever is shown as it varies with the environmental gas pressure.

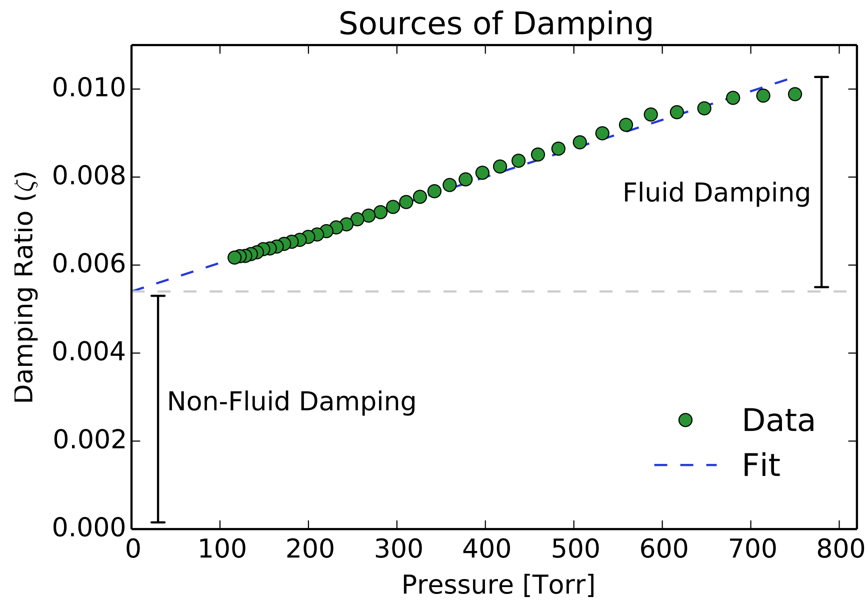

Figure 6.5 The value of the damping ratio ($\zeta = 1/(2Q)$) for a given cantilever is shown for a range of environmental gas pressures. It can be seen that at atmospheric pressure approximately half of the total damping is due to fluid damping, the other half being due to clamping and other losses.

atmospheric or fluid viscosity increases. It is likely that much of the other damping is due to clamping losses.

Chapter 7

Sensing

Cantilever resonant frequencies were measured at several levels of humidity. The cantilever was placed in an isolated gas environment with controlled humidity. The humidity was changed by means of saturated salt solutions. When an open container of a saturated salt solution is placed within a closed chamber, the local relative humidity reaches equilibrium at a value dependant on the particular salt used. In this study, a dessicant was used to obtain nearly 0% relative humidity, a saturated aqueous solution of calcium chloride ($CaCl_2$) was used to obtain approximately 34% relative humidity, and deiononized water was used to obtain nearly 100% relative humidity.

For a given cantilever beam, several resonance measurements were taken at different humidities in a randomized order. The resonance frequency of the beam was tracked continuously as it moved from one steady state value to another after the salt solution had been replaced and the local relative humidity was equilibrating.

The results of multiple resonance measurements of one cantilever exposed to three relative humidity values multiple times in randomized order is shown in Figure 7.1. This data shows that the response of the cantilever changes consistently with the relative humidity, with variance much smaller than the difference in response between the humidity levels tested. The trend observed is as expected. As relative humidity is increased, it is expected that more water molecules will adsorb

onto the available cantilever surface area [8] [9] [10] [11] [12]. These adsorbed molecules add mass to the cantilever beam, decreasing its resonant frequency. Figure 7.1 shows that the resonant frequency of the beam studied decreases at higher relative humidity levels.

The quality factor of the cantilever was also found to vary with the relative humidity, although not nearly as significantly as the resonant frequency. Although relative humidity would not be expected to have a large impact on fluid damping experienced by a cantilever, adsorbed materials would be expected to have some impact on the internal losses in a porous resonator such as thermoelastic damping (TED) [13].

The relative humidity could have some impact on the elastic modulus of the device. This effect was not explored in detail, but it is expected that the change in the mass of the beam may contribute more heavily to the change in resonant frequency of the cantilever.

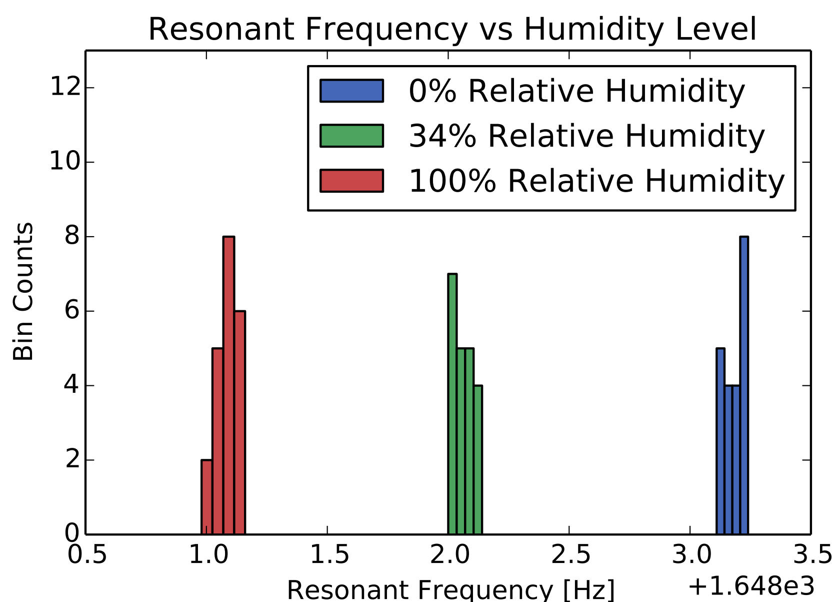

Figure 7.1 Histogram of measured resonance frequencies at various levels of humidity.

In addition to measuring cantilever responses at a humidity level steady state, beams were tracked as the humidity in the chamber changed. An example of this equilibration data can be seen

in Figure 7.2. It could be argued that the beam took a very long time to respond to a stimulus, but the cantilever responded on the same time scale as the humidity in the chamber was changed. More work is required to determine the time response of the cantilever sensor.

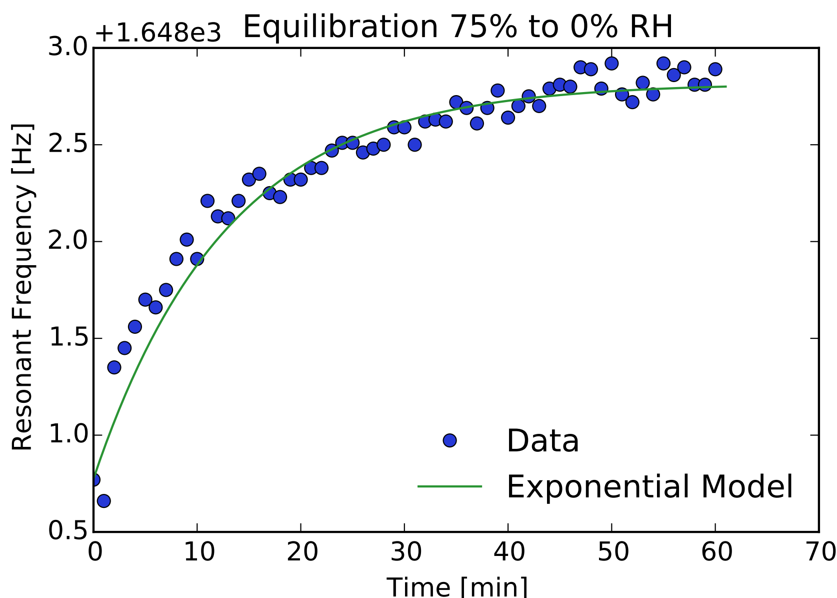

Figure 7.2 Equilibration between humidity levels

The resonant response of cantilevers was observed to vary strongly with the gas pressure of the measurement environment [14]. Many of these changes in response were expected. For example, as pressure increases, cantilever quality factor is expected to decrease as more damping is present and the device loses more energy per cycle to fluid damping forces [15]. Additionaly, as pressure increases, the resonant frequency of a cantilever resonator is expected to decrease as a result of fluid damping [16].

Both the resonant frequency and the quality factor of a given cantilever beam can be seen to vary with environment pressure in Figure 7.3. In this figure, however, note that the horizontal axis is pumping time, not pressure. This data was taken with zero time corresponding to ambient air pressure (about 680 Torr), while as pumping time goes on the pressure drops down to nearly 1 Torr.

Expected behavior for both resonant frequency and quality factor is demonstrated in this case.

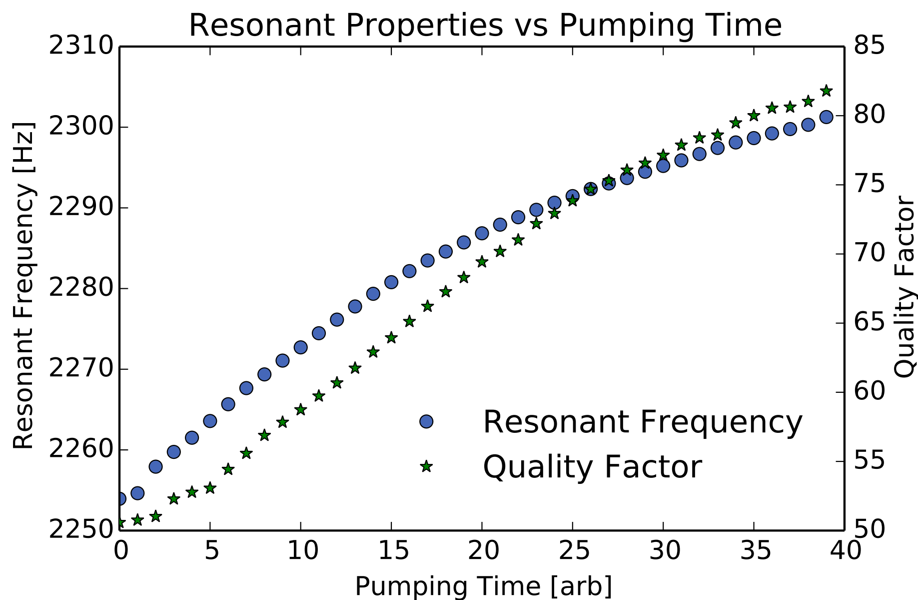

Figure 7.3 A trace of a single device resonance frequency and quality factor over time as the pressure in the chamber was lowered from atmospheric pressure to approximately 1 Torr.

Other chemicals can also be sensed. In the few hours the new testing system has been setup, initial data on sensing acetone vapor has been obtained. More work is needed to increase consistency and obtain more data, but rough preliminary results are shown in Figure 7.4

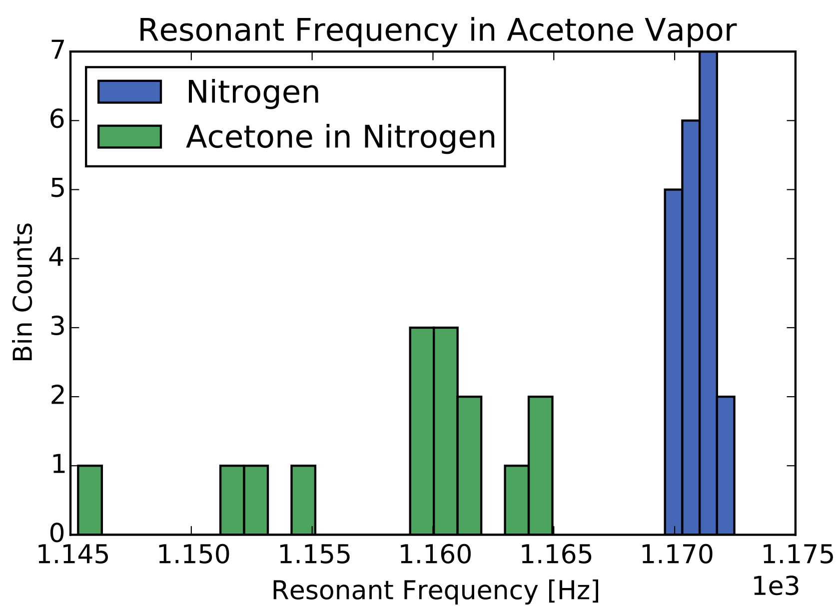

Figure 7.4 Initial attempt at sensing acetone vapor

Chapter 8

Modeling and Sensitivity Optimization

Micro-cantilevers are used as extremely accurate chemical sensors, but their performance in fluid environments has generally been poor. Making these sensors porous has the potential to increase sensitivity by up to four orders of magnitude and simultaneously allow for accurate detection in fluid environments. High aspect ratio microfabrication methods using porous materials have not previously been available, but the newly developed carbon nanotube templated microfabrication (CNT-M) process makes such fabrication possible. Proof of concept devices have been fabricated and tested, but these devices were not optimized in any way. We present the modeling and sensitivity optimization of these new devices. Our results suggest performance gains of over three orders of magnitude above the proof of concept devices. It is additionally shown that, under the applicable constraints, higher porosity and longer devices both independently offer higher sensitivities.

8.1 Nomenclature

8.1.1 Design Variables

- L is the length of the cantilever

- W is the width of the cantilever
- H is the height of the cantilever
- R is the radius of the coated carbon nanotubes after filling
- D is the distance between nearest neighbor carbon nanotubes
- A is the amplitude (the maximum cantilever tip deflection)

8.1.2 Intermediate Variables

- ρ is the effective density of the cantilever device
- E is the effective stiffness of the cantilever
- f_0 is the fundamental resonant frequency of the cantilever
- f_n is the frequency of the nth resonant mode of the cantilever
- f_{dn} is the frequency of the damped nth resonant mode of the cantilever
- f_1 is the frequency that yields the highest slope on a resonance peak
- Q is the cantilever quality factor
- S is the surface area of the porous cantilever
- x is the distance from the base along the length of the cantilever
- δ is the deflection of the cantilever
- Γ is the hydrodynamic function of the cantilever
- Re is the Reynolds number characterizing the fluid flow around the cantilever during resonance

8.1.3 Objective Function

- σ is the sensitivity, measured in response amplitude per analyte concentration

8.1.4 Constants

- ρ_f is the density of the fluid environment
- η is the viscosity of the fluid environment
- ρ_m is the density of the coating material
- d is the distance between the base of the cantilever and a base plate above which the beam is mounted

8.2 Methods and Models

Due to the unique nature of the micro-cantilevers that provide a basis for this study, models of several of their characteristics are not currently found in the literature. As a result, a large amount of first principles modeling will be presented in this section alongside variations of some models commonly in use in this field.

8.2.1 Constraints and Bounds

Variable bounds used in this study (determined by manufacturability) are:

- $500\ \mu\text{m} < L < 10$ mm
- $150\ \mu\text{m} < W < 2$ mm
- $10\ \mu\text{m} < H < 2$ mm
- $10\ \mu\text{m} < R < 1$ mm
- $50\ \mu\text{m} < D < 150\ \mu\text{m}$
- $0\ \text{mm} < A < 1$ mm

Constraints used in the optimization are:

- $R < \frac{D}{\sqrt{3}}$
- $A \leq \frac{L}{10}$
- $A \leq \frac{d}{2}$

These constraints respectively prevent the beam from being more than entirely filled with material, limit the amplitude in order to prevent cantilever failure or nonlinear resonance effects, and limit the amplitude such that the beam will not come into contact with the base plate it is mounted above.

8.2.2 Gaussian Windowing

A method was developed and implemented that will be referred to as Gaussian Windowing. This method is an alternative to spline based or k-weighted interpolation methods. The advantage of this method is that it is not simply a mathematical construct, but rather has a great deal of physical relevance.

Models of physical systems that are discontinuous or not differentiable prove difficult for optimization methods. Since physical systems rarely exhibit discontinuity or non-differentiability on a bulk scale, it could be claimed that a model with these features is inherently flawed. This is not always the case, however. Physical systems do often exhibit these sharp transitions on a small scale due to the nature of quantum mechanics, but bulk systems rarely show these features due to decoherence or, more generally, variance.

Gaussian Windowing samples a (possibly discontinuous or non-differentiable) model function at multiple points and returns a gaussian weighted average of the results. This effectively models variance in the intermediate model variables, which indeed is always present, with the standard deviation often known through experimental experience with the system.

Use of this method is demonstrated in the following section. It should be noted that this method not only produces models with continuous gradients for use in gradient based optimization, but it

also has the potential to create physically accurate models from inaccurate models that assume no variance, regardless of whether the model is then used for optimization purposes.

8.2.3 Surface Area vs Coating Radius

Assume the carbon nanotubes are hexagonal close packed. This model will look at the surface area contributed by one coated carbon nanotube of total radius R where the distance between carbon nanotubes is D.

The growing surface area is then

$$s_g = 2\pi RH$$

If the shrinking surface area is approximated by flat edges rather than arcs, then

$$s_s = 6\left(2D - \frac{4R}{\sqrt{3}}\right)H$$

The maximum value of R, R_{max}, will occur when $S_s = 0$, so

$$R_{max} = \frac{D}{\sqrt{3}}$$

If arcs are treated properly, then

$$c = 2D - \frac{4R}{\sqrt{3}}$$

$$s_s = 6\left(2R\sin^{-1}\left(\frac{c}{2R}\right)\right)H$$

$$s_s = 6\left(2R\sin^{-1}\left(\frac{D}{R} - \frac{2}{\sqrt{3}}\right)\right)H$$

These two surface area models, s_g and s_s, are each active in a separate regime. s_g is the correct model for $R < \frac{D}{2}$, while s_s is the correct model for $R > \frac{D}{2}$. It is necessary to combine these two models together, but doing so in a piecewise manner would result in a non-differentiable function. Multiple methods exist for combining them more correctly, such as gaussian windowing.

Plotting these functions for typical values of the constants yields the plot shown in Figure 8.1.

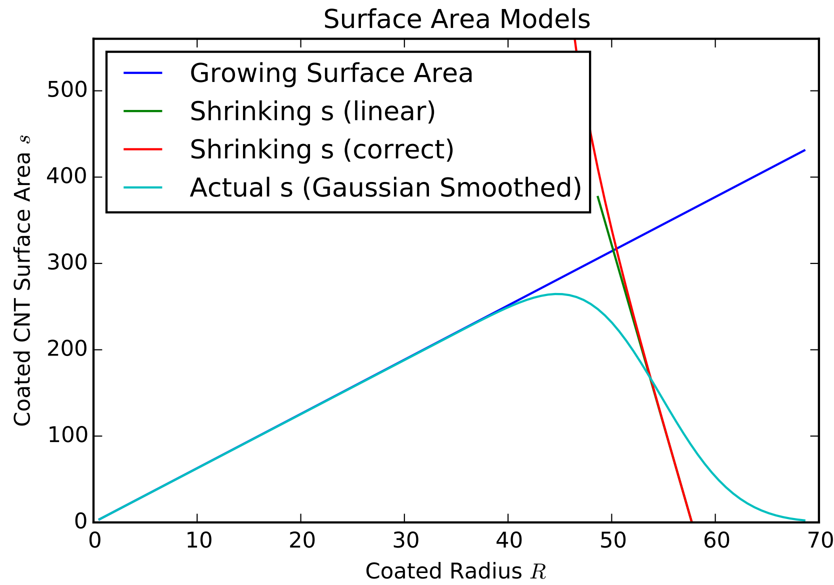

Figure 8.1 Graph of surface area models created from circular assumption.

We then must find the number of nanotubes in the beam. Assuming the carbon nanotubes are hexagonal close packed, the distance between each nanotube is related to the side length of the hexagon in which it resides by

$$D = 2\left(\frac{\sqrt{3}}{2}a\right)$$

or, solving, we have

$$a = \frac{D}{\sqrt{3}}$$

The area of the hexagon belonging to each nanotube is then

$$A_{CNT} = \frac{3\sqrt{3}}{2}a^2 = \frac{\sqrt{3}}{2}D^2$$

The number of nanotubes per cantilever (N_{CNT}) can then be estimated by the base area of the cantilever ($L*W$) divided by the area occupied by each nanotube as follows:

$$N_{CNT} = \frac{LW}{A_{CNT}} = \frac{2LW}{\sqrt{3}D^2}$$

The surface area of the beam is then given by the surface area of one coated carbon nanotube multiplied by the number of nanotubes in the beam, or

$$S = N_{CNT} * s = \frac{2LW}{\sqrt{3}D^2}s$$

8.2.4 Material Occupied Volume

The simplest model of the volume occupied by material (not including pores) that avoids collision issues is that of a hexagonal linear approximation. If each coated carbon nanotube is approximated as a hexagon, then the volume of a coated nanotube is

$$v_m = \frac{3\sqrt{3}}{2}R^2H$$

This leads to the entire material occupied volume being represented by

$$V_m = N_{CNT} * v_m = \frac{3\sqrt{3}}{2}N_{CNT}R^2H$$

A more accurate model is given by properly treating the intersection of cylinders. To find the intersection area of two circles of radius R and distance between centers, D, we must first find the angle θ subtended by the two radii that define the sector in which intersection occurs. An isosceles

triangle is formed by these two radii and the corresponding chord. This triangle can be divided into two right triangles with hypotenuse R and one side length of $D/2$, with the remaining side having a length half that of the chord. The angle of this triangle which stems from the center of the circle is then given by

$$\cos^{-1}\left(\frac{D}{2R}\right)$$

such that the angle of interest is twice that given above, or

$$\theta = 2\cos^{-1}\left(\frac{D}{2R}\right)$$

The area of the sector is then given by

$$A_{sect} = \frac{\theta}{2}R^2 = \cos^{-1}\left(\frac{D}{2R}\right)R^2$$

Before computing the area of the isosceles triangle, we must know the chord length. Using the Pythagorean theorem on the right triangle, we have

$$\left(\frac{D}{2}\right)^2 + \left(\frac{c}{2}\right)^2 = R^2$$

leading to

$$c = \sqrt{4R^2 - D^2}$$

The area of the isosceles triangle is then given by

$$A_{tri} = \frac{1}{2}c\frac{D}{2} = \frac{D}{4}\sqrt{4R^2 - D^2}$$

Since the intersection area is the difference between the area of the sector and the area of the isosceles triangle, we now have a accurate equation to model for when the nanotubes begin to

touch each other.

$$\begin{aligned} A_{int} &= A_{sect} - A_{tri} \\ &= \cos^{-1}\left(\frac{D}{2R}\right) R^2 - \frac{D}{4}\sqrt{4R^2 - D^2} \end{aligned}$$

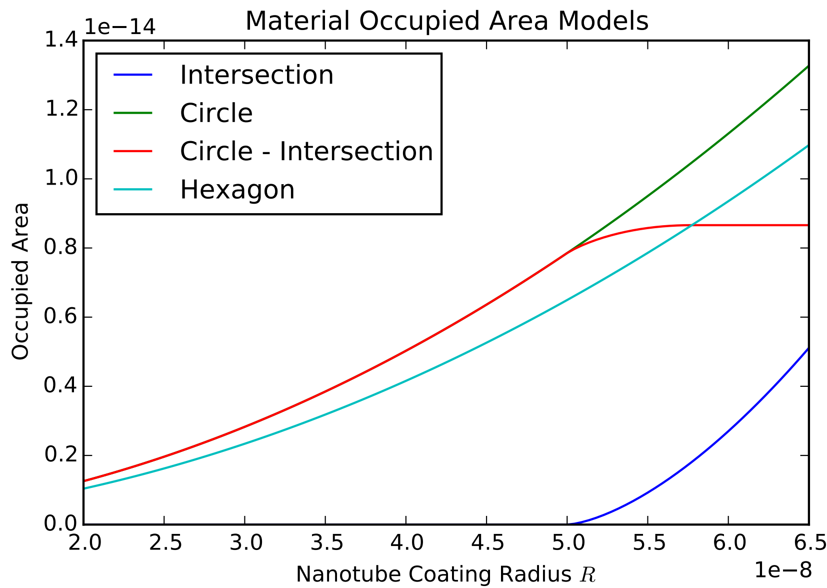

Figure 8.2 Plot of area occupied by the nanotubes in a horizontal cross-section. Comparing the circular intersecting model with the hexagonally close packed model.

8.2.5 Device Density

The device density ρ (dependent on the material density ρ_m) varies simply with the volume occupied by material V_m.

The mass of the cantilever will be equal to the density of the material ρ_m multiplied by the material occupied volume V_m, and the density of the cantilever device will be its mass divided by its volume which is simply equal to LWH, so for the device density we have

$$\rho = \frac{\rho_m V_m}{LWH}$$

8.2.6 Device Elastic Modulus

The Young's Modulus of the cantilever beam can be obtained through existing models of the modulus of porous materials [17].

One simple model of the elastic modulus of a porous material is

$$E = E_m \left(1 - \frac{p}{p_c}\right)^f$$

where p is the porosity (occupied volume over total volume), p_c is the critical porosity beyond which the modulus is zero (assumed 1 for our model), E_m is the elastic modulus of the material, and f is an empirical factor that is material dependent (values typically range from 1 to 2, a value of 1.5 was used in this model) [18]. The figure below shows the relationship between porosity and elastic modulus.

8.2.7 Resonant Frequency

For a simple, undamped beam, the mode resonant frequencies can be found through solution of the cantilever differential equation to be

$$f_n = \frac{k_n^2}{2\pi} \frac{H}{L^2} \sqrt{\frac{E}{12\rho}}$$

Where the values of k_n are the solutions to the trancendental equation

$$1 + \cos(k_n)\cosh(k_n) = 0$$

The first four k_n values, for reference, are shown in Table 8.1.

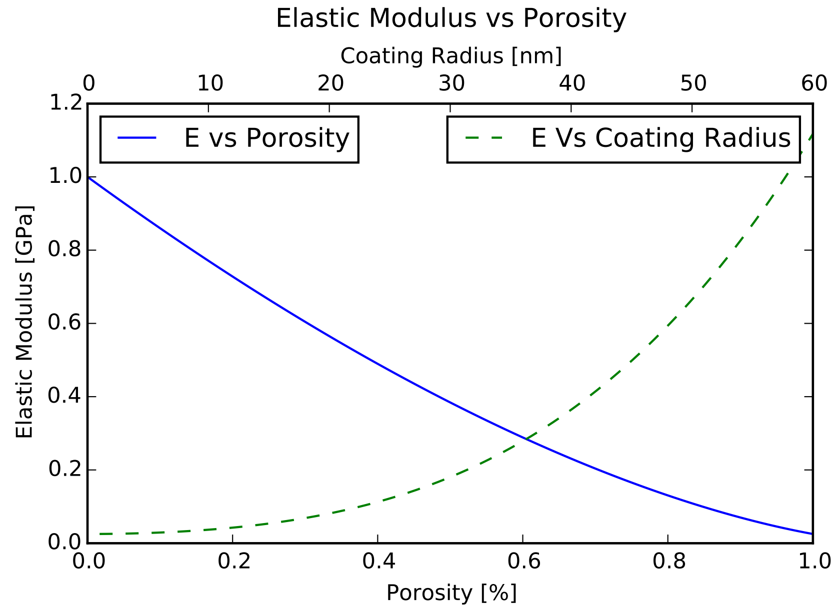

Figure 8.3 Plot of the elastic modulus as a function of the porosity of the carbo-nanotube beam.

k_n	Value
k_0	1.87510406871
k_1	4.69409113297
k_2	7.85475743824
k_3	10.9955407349

Table 8.1 The first four constants used in the resonant frequency equation to find different modes

8.2.8 Damped Resonant Frequency

The above results give the undamped resonant frequency. Damping not only alters the quality factor, but also the resonant frequency. Thus, the damped resonant frequency depends on the extent of damping, which can be portrayed through the quality factor. These damped resonant frequencies are given by

$$f_{d0} = \frac{k_n^2}{2\pi} \frac{H}{L^2} \frac{Q}{\sqrt{3+12Q^2}} \sqrt{\frac{E}{\rho}}$$

This relation comes from solving the cantilever differential equation with a linear damping term and substituting in the quality factor for the damping term by comparing the obtained ring-down decay rate in the solution to the definition of the quality factor.

8.3 Resonant Mode Shapes

The undamped mode shapes can be found by solving the cantilever differential equation, and are given by

$$\delta(x) = A\left(C_1 + \frac{-\cos(k_n) - \cosh(k_n)}{\sin(k_n) + \sinh(k_n)} C_2\right)$$

where

$$C_1 = \cos\left(\frac{k_n x}{L}\right) - \cosh\left(\frac{k_n x}{L}\right)$$

and

$$C_2 = \sin\left(\frac{k_n x}{L}\right) - \sinh\left(\frac{k_n x}{L}\right)$$

8.3.1 Hydrodynamic Function

The hydrodynamic function for a circular beam can be found analytically [19] [20] to be

$$\Gamma_{circ}(\omega) = 1 + \frac{4iK_1(-i\sqrt{iRe})}{\sqrt{iRe}K_0(-i\sqrt{iRe})}$$

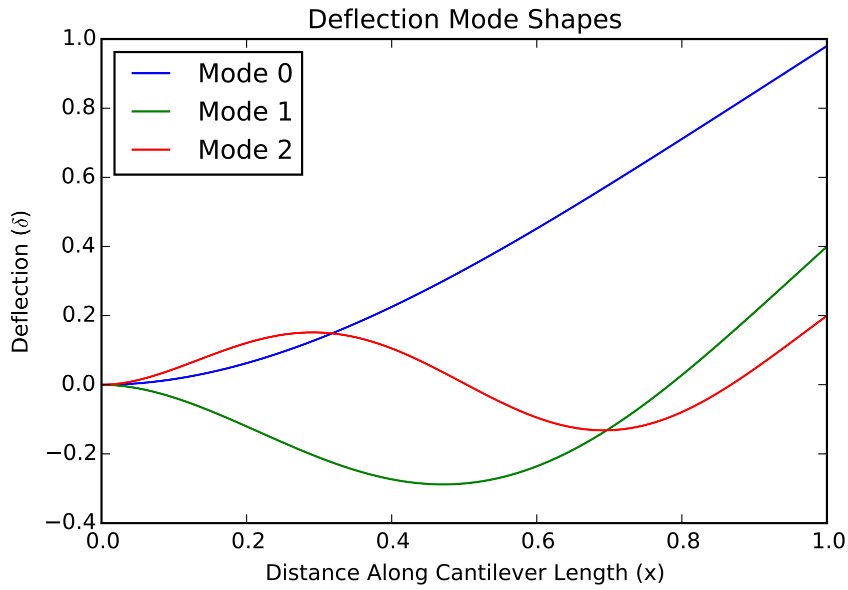

Figure 8.4 Plot of the deflection shape for each of the three first resonant modes of a cantilever beam

This analytic result can then be corrected [19] to show that the hydrodynamic function of a rectangular beam is given by

$$\Gamma_{rect}(\omega) = \Omega(\omega) * \Gamma_{circ}(\omega)$$

where

$$\Omega(\omega) = \Omega_r + i\Omega_i$$

$$\Omega_r = \frac{\sum_{i=0}^{6} C_i \tau^i}{1 + \sum_{i=7}^{12} C_i \tau^{i-6}}$$

$$\Omega_i = \frac{\sum_{i=13}^{18} C_i \tau^{i-13}}{1 + \sum_{i=19}^{2} 4C_i \tau^{i-18}}$$

$$\tau = log(Re)$$

and the constants C_n, in order from C_0 to C_{24} are: 0.91324, −0.48274, 0.46842, −0.46842, 0.044055, −0.0035117, 0.00069085, −0.56964, 0.4689, −0.13444, 0.045155, −0.0035862, 0.00069085, −0.024134, −0.029256, 0.016294, −0.00010961, 0.000064577, −0.000044510, −0.59702, 0.55182, −0.18357, 0.0079156, −0.014369, and 0.0028361 [19].

8.3.2 Reynolds Number

The Reynolds number for the fluid flow around the beam is given by [19] to be

$$Re = \frac{\pi \rho_f f_0 W^2}{2\eta}$$

8.3.3 Quality Factor

The quality factor of the beam effects sensitivity by determining the sharpness of the resonant peak. The quality factor, Q, is defined as

$$Q = 2\pi \frac{\text{Energy in the Mode}}{\text{Energy Lost per Cycle}}$$

Since the damped resonant frequency has been shown previously to be given by

$$f_{d0} = \frac{k_n^2}{2\pi}\frac{H}{L^2}\frac{Q}{\sqrt{3+12Q^2}}\sqrt{\frac{E}{\rho}}$$

we can solve for the quality factor to obtain

$$Q = \sqrt{\frac{3}{b^2 - 12}}$$

where

$$b = \frac{k_n^2}{2\pi f_{d0}} \frac{H}{L^2} \sqrt{\frac{E}{\rho}}$$

Then, since the damped resonant frequency is also given by

$$f_{d0} = \frac{f_0}{\sqrt{1 + \frac{\pi \rho_f W}{4 \rho H} \Gamma_r}}$$

We can then simplify the expression for b to obtain

$$b = \sqrt{12 + \frac{3\pi \rho_f W}{\rho H} \Gamma_r}$$

which, together with the above results, determines the quality factor. This result can be seen plotted against several variables in Figure 8.5.

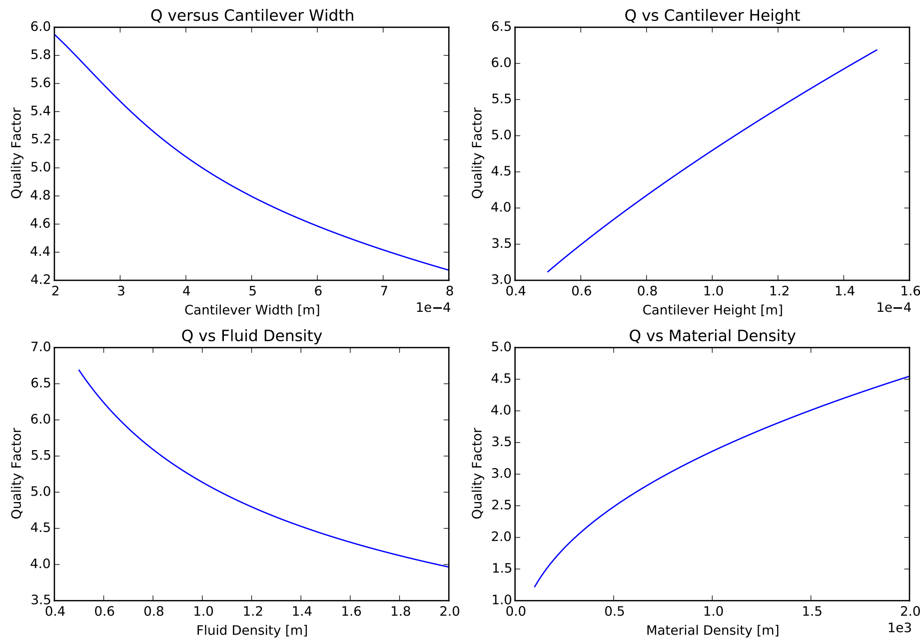

Figure 8.5 Assortment of plots showing the how changing each design variable will effect the quality factor of the beam

Four other models for the quality factor were explored. Some showed similar behavior, while some began producing results but need additional work to become viable models. The models not

presented are much more complex, and should correspondingly offer more accurate results when completed. The results of these models will be presented in a future work.

8.3.4 Lorentzian Amplitude

When the cantilever is treated as a simple harmonic oscillator, the response amplitude function is given by the following Lorentzian curve

$$A = \frac{A_0}{\sqrt{\left(\frac{ff_0}{Q}\right)^2 + \left(f_0^2 - f^2\right)^2}}$$

The first derivative of this function is

$$\frac{dA}{df} = -\frac{A_0\left(4f^3 + 2ff_0^2\left(\frac{1}{Q^2} - 2\right)\right)}{2\left(f^4 + f^2 f_0^2\left(\frac{1}{Q^2} - 2\right) + f_0^4\right)^{3/2}}$$

The second derivative is

$$\frac{d^2A}{df^2} = A_0 \frac{t_0 + 6f^6Q^4 + 5f^4 f_0^2 Q^2\left(1 - 2Q^2\right)}{t_1\sqrt{f^4 + f^2 f_0^2\left(\frac{1}{Q^2} - 2\right) + f_0^4}}$$

where

$$t_0 = 2f^2 f_0^4\left(Q^4 - 4Q^2 + 1\right) + f_0^6 Q^2\left(2Q^2 - 1\right)$$

and

$$t_1 = \left(Q^2\left(f^2 - f_0^2\right)^2 + f^2 f_0^2\right)^2$$

Solving for where the second derivative is zero and identifying which of the solutions corresponds to a global maximum in the first derivative yields the frequency f_1 at which maximal slope

magnitude is obtained (t_0, (t_1 and t_2 are terms used as intermediate expressions to simplify the final statement)

$$t_0 = -6144Q^{10} + 8208Q^8 - 7752Q^6 + 3729Q^4$$

$$t_1 = \sqrt{t_0 - 828Q^2 + 69}$$

$$t_2 = \sqrt[3]{-512Q^6 + 1416Q^4 - 870Q^2 + 18t_1 + 145}$$

$$f_1 = \frac{f_0}{3Q}\sqrt{\frac{64Q^4 - 5t_2 + t_2^2 + 2Q^2\left(5t_2 + 22\right) - 11}{2t_2}}$$

The maximal value of the slope is then given simply by $\frac{dA}{df}(f1)$

Using a linear approximation about the resonance frequency, we have the approximation

$$A = A_1 + \frac{dA}{df}(f1)\Delta f$$

Since the derivative of the resonance frequency with mass is given by

$$\frac{df_0}{dm} = -\frac{k_0^2}{4\pi}\frac{H}{L^2}\sqrt{\frac{ELWH}{12m^3}}$$

The frequency shift Δf is then given with another linear approximation by

$$\Delta f = -\frac{k_0^2}{4\pi}\frac{H}{L^2}\sqrt{\frac{ELWH}{12m^3}}\Delta m$$

Substituting this result into the previous expression for the amplitude at the point of maximal slope provides

$$A = A_1 - \frac{dA}{df}(f1)\frac{k_0^2}{4\pi}\frac{H}{L^2}\sqrt{\frac{ELWH}{12m^3}}\Delta m$$

The change in mass is proportional to the surface area of the cantilever and the concentration of the chemical to be sensed

$$\Delta m \propto [m]S$$

When substituted assuming equality rather than proportionality, this leads to

$$A = A_1 - \frac{dA}{df}(f1)\frac{k_0^2}{4\pi}\frac{H}{L^2}\sqrt{\frac{ELWH}{12m^3}}[m]S$$

The maximum value of this amplitude function is given by

$$A_{max} = \frac{Q}{4\pi^2 f_0^2}$$

The amplitude function can be normalized by this maximum value if desired.

8.3.5 Sensitivity

Many of the previously discussed characteristics of the beam that have been modeled could be considered objectives in their own right. For example, it is desirable to maximize the quality factor of a sensor, while it is also desirable to minimize the mass of the sensor. It was initially unclear how these separate aspects of the beam could be brought together into a single objective. We determined that the sensitivity of the sensor is the most important objective that relies on all other characteristics of the device. Our model for sensitivity follows.

Sensitivity (σ) is the objective to be optimized. It is dependent upon each other model of cantilever behavior presented in the previous sections.

Sensitivity is essentially how much the measured amplitude changes for a given change in the concentration of the chemical to be sensed. This concept can be visualized in Figure 8.6, where as mass adsorbs onto a cantilever beam that is being driven at frequency f_1, the added mass causes

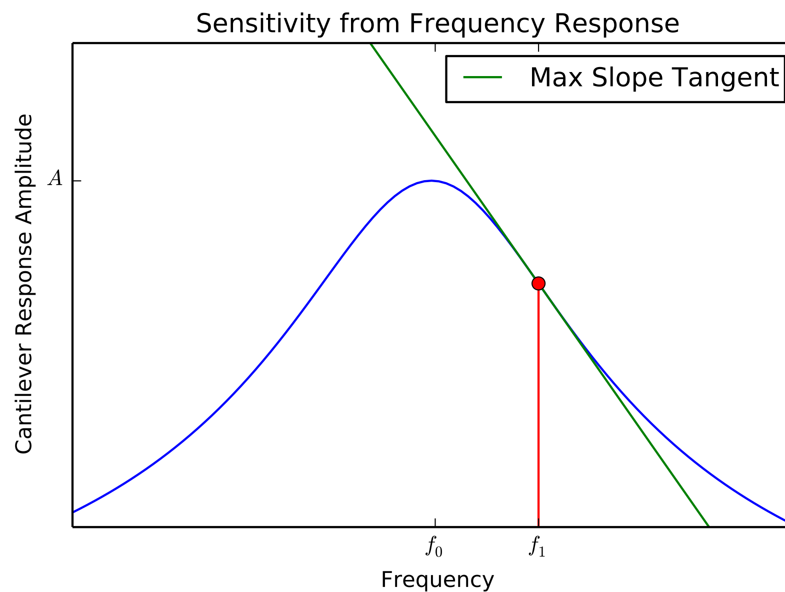

Figure 8.6 Plot showing the critical concept in micro-cantilever sensors. f_1 is the frequency at which the change in amplitude of the beam has the greatest slope. The steeper the slope the more sensitive the beam will be.

the resonance peak to shift to lower frequencies, causing a change in output proportional to the frequency response function slope (the red dot moves along the green line in Figure 8.6). This can be stated more formally as

$$\sigma = \frac{dA}{d[m]}$$

And, using the first approximation found in the Lorentzian Amplitude section, leads to

$$\sigma = -\frac{dA}{df}(f1)\ \frac{k_0^2}{4\pi}\frac{H}{L^2}\sqrt{\frac{ELWH}{12m^3}}S$$

8.3.6 Optimization

An interface sensitivity function was designed to take rescaled design variables and send the scaled versions into the original sensitivity function, afterward returning the negative of the rescaled result

(proper for minimization, since sensitivity is to be maximized). The variable values and objective values are also stored for future reference and analysis such as tracking the optimizer path through parameter space or creating convergence plots.

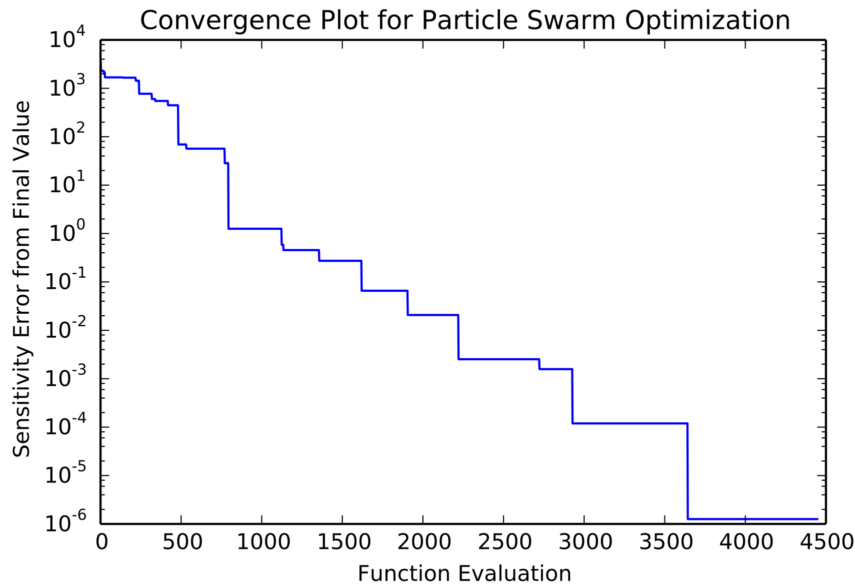

Figure 8.7 Plot showing the change in sensitivity error over the life span of the particle swarm optimization

Rescaling design variable values and sensitivity values to order one proved extremely important in obtaining reliable results from the optimizers.

Two primary optimization algorithms were used: Particle Swarm Optimization (PSO) and a modified limited memory Broyden-Fletcher-Goldfarb-Shanno (L-BFGS) method that properly handles bounds and constraints. PySwarm was the PSO implementation used, and the SciPy optimization package provided the BFGS implementation.

A convergence plot indicating the performance of the PSO algorithm can be seen in Figure 8.7, while a similar plot indicating the performance of the BFGS algorithm on this problem can be seen in Figure 8.8. The BFGS algorithm took largely fewer function calls to converge, and this improvement increases when automatic differentiation is used in place of finite differencing.

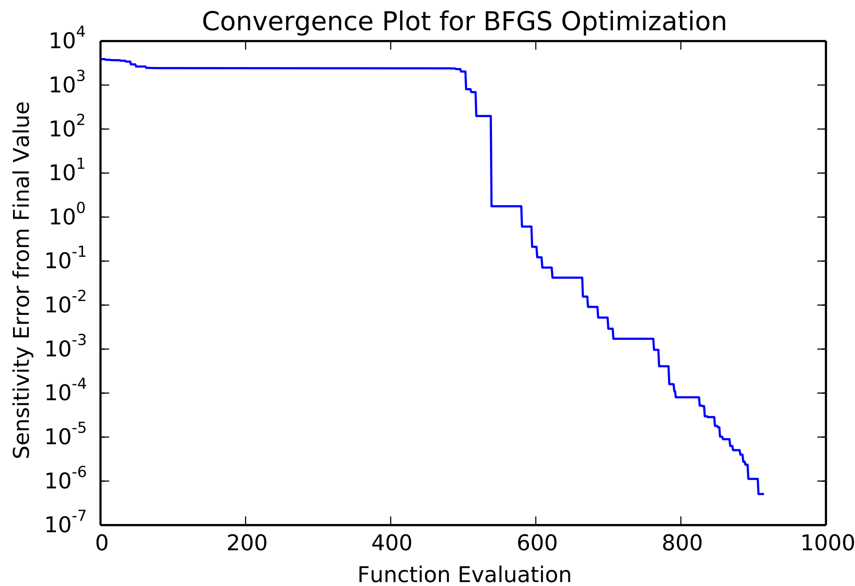

Figure 8.8 Plot showing the convergence for BFGS optimization sensitivity

Finite differencing was primarily used to provide gradients to the BFGS optimization method. Automatic differentiation was also implemented using the "AD" python package. This improved gradient source will be used in future work in this area to improve the speed and accuracy of the BFGS optimization method or other gradient optimization implementations that will be explored in future work.

8.4 Results

Due to the unique nature of the devices studied, the models describing their characteristics in terms of fabrication controllable variables is a feat and a result in its own right.

The unification of many aspects of micro-cantilever sensor function into one central objective, sensitivity, offers many insights to the field that have previously not been frequently implemented. For this reason, the dependence of sensitivity on the design variables is presented as a result rather than a premise.

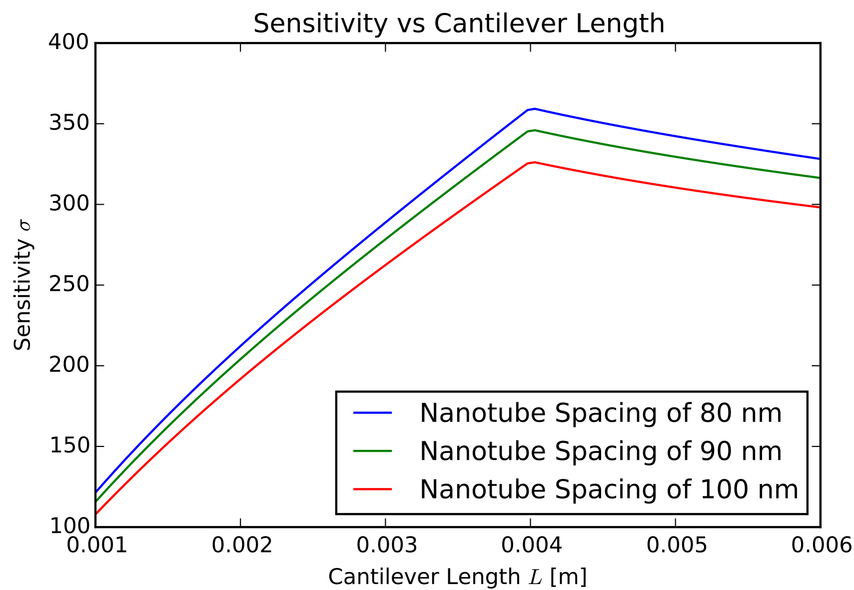

Figure 8.9 Plot showing the relationship between the length of the beam and its sensitivity

It can be seen in Figure 8.9 that sensitivity increases with cantilever length for a porous device. At a critical length the sensitivity begins to decrease with length. This occurs because the plotted values are the optimum sensitivity values with the indicated variables fixed, and an amplitude constraint becomes active at transition point. The basics of this result shows the longer the better but the constraint is inhibiting extra long micro-cantilever beams.

In Figure 8.10 it can be seen that the sensitivity tends to lower values the wider the beam becomes. This is a result of higher fluid drag forces on wider cantilever beams. Therefore the thinner the better.

Figure 8.11 shows that the taller the nanotube beams are manufactured the more sensitive the beam will become. This trend is a result of thicker cantilevers having more energy in their resonant mode and thus a higher quality factor. In contrast to the width, an increase in height will not significantly increase the fluid drag. Note that this increase in sensitivity with height is only possible for porous sensors. For a solid sensor, increased thickness would quickly lead to the

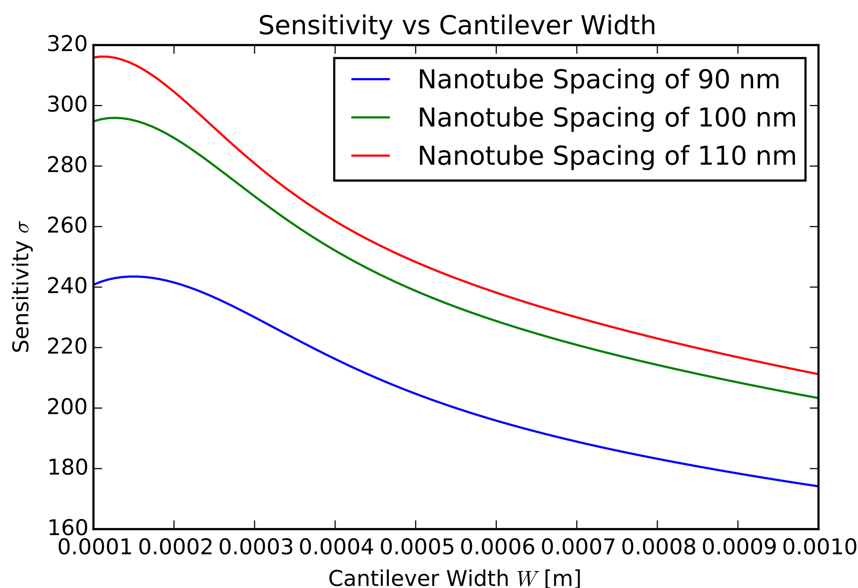

Figure 8.10 Plot showing the relationship between the width of the beam and its sensitivity

mass of the sensor overpowering the mass of the analyte. Solid sensors must resultingly be made extremely thin, but porous sensors can gain great increases in sensitivity by moving to thicker geometries.

Figure 8.12 shows clearly that the constraint to have a large enough spacing between nanotubes relative to the coating radius must be satisfied, and also that an optimum value would be expected to lie near the median of feasible values.

As can be seen in Figure 8.13, an optimal coating radius appears in the middle of the range of feasible values. This would be expected because it follows expectations of surface area dependence. A surprising result was found, however, when constraints were added as can be visualized in Figure 8.14. Here the optimum sensitivity is plotted where optimization occurred with indicated variables (coating radius and nanotube spacing) fixed. Under the influence of the constraints, the profile is such that smaller coating radii are more favorable. This means that with constraints considered, optimal devices should be made as porous as is possible under the appropriate bounds,

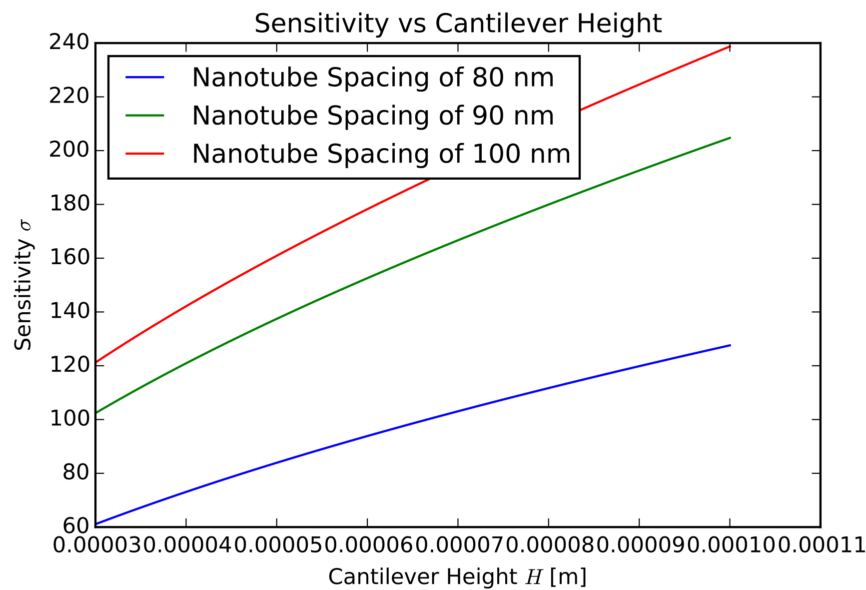

Figure 8.11 Plot showing the relationship between the height of the beam and its sensitivity

strengthening the position of porous devices.

The optimizers used performed well and produced results consistent with each other. Under optimization, all design variables were pushed up against bounds or constraint barriers. Although this is not uncommon for such problems, it was an unexpected result for this particular problem. Several of the design variables were expected to have intermediate optimum values, but interaction effects and constraints caused this to not be the case.

Although this behavior can at times be the result of an optimizer exploiting a flaw in a model, after careful scrutiny this was not found to be the cause in this case. In contrast, the optimizer was pointing out correct results that had not been intuitive and thus had not been considered.

As a general rule we discovered that the longer, taller, thinner and more porous you can manufacture a carbon nanotube scaffolded micro-cantilever the more sensitive it will be as a chemical concentration sensor.

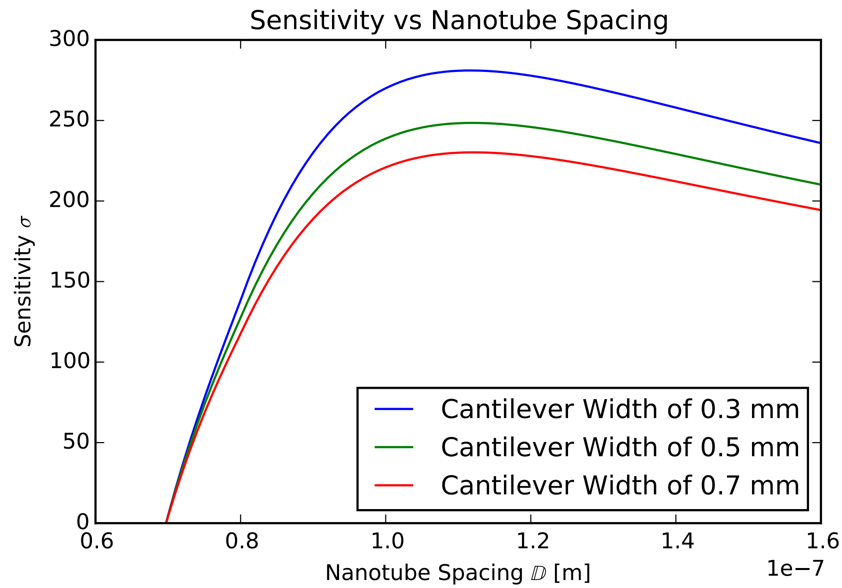

Figure 8.12 Plot showing the relationship between the spacing of each nanotube and the beams sensitivity.

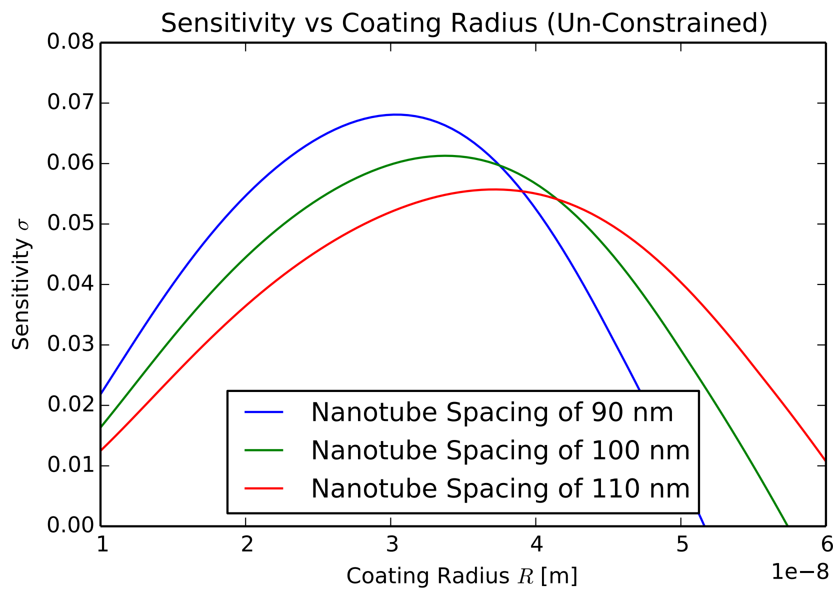

Figure 8.13 Plot showing the unconstrained relationship between the coating radius of the beam and its sensitivity.

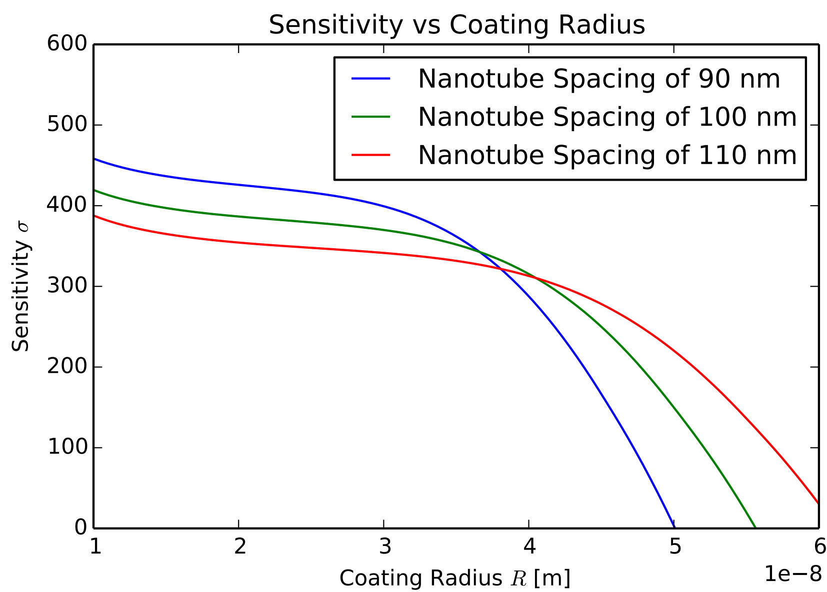

Figure 8.14 Plot showing the relationship between the coating radius of the beam and its sensitivity.

8.5 Optimization Conclusion

The modeling and optimization presented here show that previously fabricated proof of concept porous cantilever sensors have been created with far from optimal parameters. This optimization proposes that the sensitivities of these initial devices could be improved by up to three orders of magnitude.

In addition, the interactions modeled here show that some trends in the microcantilever sensor field may be moving in non optimal directions. For example, many cantilevers are moving toward shorter geometries, while we suggest (at least for porous sensors) that optimization would suggest moving toward longer beams. Also, thin beams prevail in the field, but these results suggest that thick porous beams could have orders of magnitude higher performances.

Expected trends were confirmed and new insights pointed out by the optimizers, offering a great deal to the field of microcantilever chemical concentration sensing.

Chapter 9

Conclusion

The porous cantilever resonant sensors studied in this work show promise in offering advantages in the field of chemical concentration sensing. Fabrication has been shown to be successful and flexible. High aspect ratios have been obtained, and variable porosities acheived. Physical and resonant properties of the fabricated devices were characterized. Thermo Elastic Dampening (TED) was found not to be dominant in environments of interest. Changes in cantilever resonant response were shown for variable environmental conditions such as pressure and relative humidity.

9.1 Future Work

In order to diversify elements in a cantilever array, each cantilever could be coated with a layer of material that promotes adhesion of a particular chemical to be sensed. Coating materials were not studied in this work, but other work has been done in this arena. Future work could explore the application and effects of coating materials on these porous cantilever sensors.

In this work, several device geometries were tested, and numerical optimization was performed, but no physical optimization took place. If such optimization were to be carried out, clamping and drag losses could be minimized, increasing device performance. In addition, an optimal porosity

could be confirmed.

Diffusion times could pose a challenge for porous sensors if they are overly long. Determination of diffusion times into these porous beams would be a valuable addition to this work.

The relationship between cantilever porosity and chemical sensitivity was discussed, but is in need of experimental confirmation.

Appendix A

Carbon Nanotube Growth Studies

Figure A.1 shows samples placed at different locations in the furnace. All samples were identical, prepared with 4 nm paterned iron catalyst atop 30 nm alumina on native silicon. It can be seen that the center of the furnace is not necessarily the ideal sample placement location. Slightly downstream of center can have higher growth rates with higher consistency. Note that distances here are measured from the inside of the ceramic ledge that supports the quartz tube.

Figure A.2 investigates the re-use of a substrate for consecutive growths. Between each growth, previous nanotubes were measured and removed. Iron loss and iron carbon contamination may be primary causes of the decreased growth rate in consecutive runs.

The results shown in Figure A.3 were obtained by setting both the hydrogen flow rate and the ethylene flow rate to the sccm value indicated in the plot during growth. As a result, the gas mixture composition was retained while total gas flow rate was adjusted.

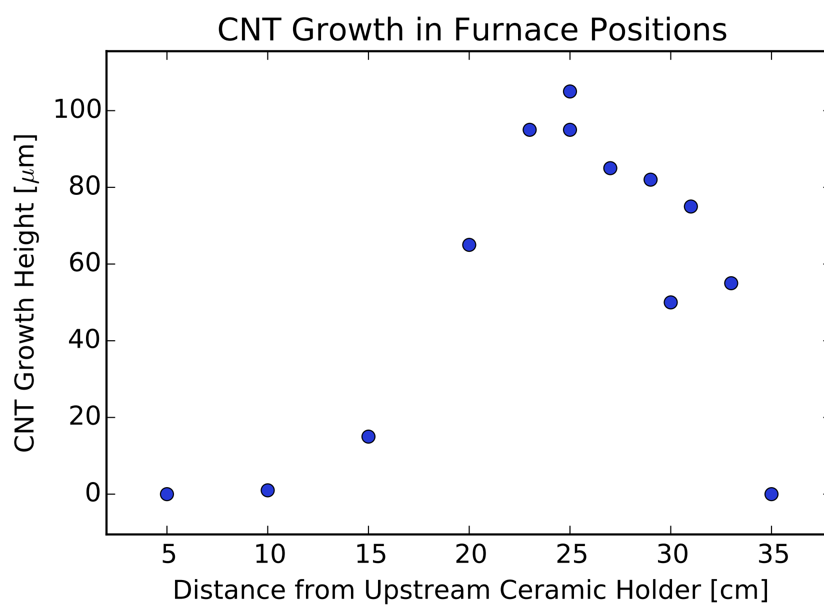

Figure A.1 CNT growth rate versus furnace placement position

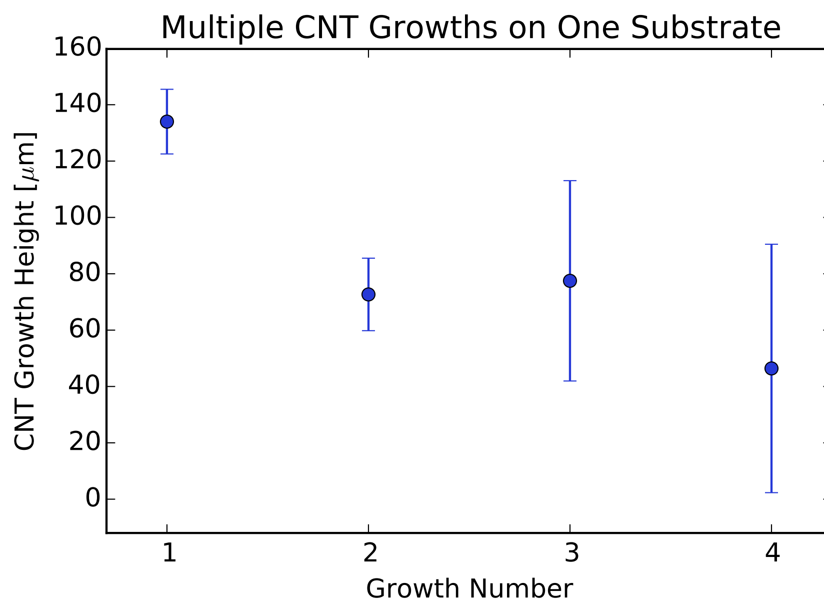

Figure A.2 CNT growth heights when the same substrate is used for multiple growths

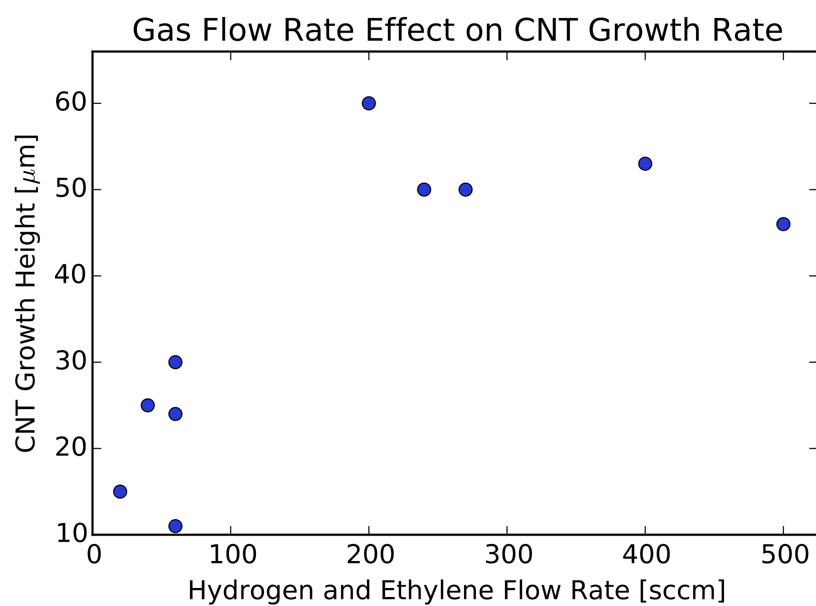

Figure A.3 Effect of total gas flow rate on CNT growth rate

Bibliography

[1] P. S. Waggoner and H. G. Craighead, "Micro-and nanomechanical sensors for environmental, chemical, and biological detection," Lab on a Chip **7,** 1238–1255 (2007).

[2] F. Battiston, J.-P. Ramseyer, H. Lang, M. Baller, C. Gerber, J. Gimzewski, E. Meyer, and H.-J. Güntherodt, "A chemical sensor based on a microfabricated cantilever array with simultaneous resonance-frequency and bending readout," Sensors and Actuators B: Chemical **77,** 122–131 (2001).

[3] Y. Yang, C. Callegari, X. Feng, K. Ekinci, and M. Roukes, "Zeptogram-scale nanomechanical mass sensing," Nano letters **6,** 583–586 (2006).

[4] Y. Hwang, F. Gao, A. J. Hong, and R. N. Candler, "Porous silicon resonators for improved vapor detection," Microelectromechanical Systems, Journal of **21,** 235–242 (2012).

[5] D. N. Hutchison, N. B. Morrill, Q. Aten, B. W. Turner, B. D. Jensen, L. L. Howell, R. R. Vanfleet, and R. C. Davis, "Carbon nanotubes as a framework for high-aspect-ratio MEMS fabrication," Microelectromechanical Systems, Journal of **19,** 75–82 (2010).

[6] J. Song, D. S. Jensen, D. N. Hutchison, B. Turner, T. Wood, A. Dadson, M. A. Vail, M. R. Linford, R. R. Vanfleet, and R. C. Davis, "Carbon-Nanotube-Templated Microfabrication of Porous Silicon-Carbon Materials with Application to Chemical Separations," Advanced Functional Materials **21,** 1132–1139 (2011).

[7] L. K. Barrett, D. J. Barton, S. G. Noyce, D. D. Allred, R. R. Vanfleet, and R. C. Davis, "High-Aspect-Ratio Metal Microfabrication by Nickel Electroplating of Patterned Carbon Nanotube Forests," (2014).

[8] P. Cao, K. Xu, J. O. Varghese, and J. R. Heath, "The microscopic structure of adsorbed water on hydrophobic surfaces under ambient conditions," Nano letters **11,** 5581–5586 (2011).

[9] K. Klier and A. Zettlemoyer, "Water at interfaces: molecular structure and dynamics," Journal of Colloid and Interface Science **58,** 216–229 (1977).

[10] A. Verdaguer, G. Sacha, H. Bluhm, and M. Salmeron, "Molecular structure of water at interfaces: Wetting at the nanometer scale," Chemical reviews **106,** 1478–1510 (2006).

[11] R. Major, J. Houston, M. McGrath, J. Siepmann, and X.-Y. Zhu, "Viscous water meniscus under nanoconfinement," Physical review letters **96,** 177803 (2006).

[12] D. B. Asay and S. H. Kim, "Evolution of the adsorbed water layer structure on silicon oxide at room temperature," The Journal of Physical Chemistry B **109,** 16760–16763 (2005).

[13] R. N. Candler *et al.*, "Impact of geometry on thermoelastic dissipation in micromechanical resonant beams," Microelectromechanical Systems, Journal of **15,** 927–934 (2006).

[14] J. Mertens, E. Finot, T. Thundat, A. Fabre, M.-H. Nadal, V. Eyraud, and E. Bourillot, "Effects of temperature and pressure on microcantilever resonance response," Ultramicroscopy **97,** 119–126 (2003).

[15] F. Blom, S. Bouwstra, M. Elwenspoek, and J. Fluitman, "Dependence of the quality factor of micromachined silicon beam resonators on pressure and geometry," Journal of Vacuum Science & Technology B **10,** 19–26 (1992).

[16] C. A. Van Eysden and J. E. Sader, "Resonant frequencies of a rectangular cantilever beam immersed in a fluid," Journal of applied physics **100,** 114916 (2006).

[17] W. Pabst, E. Gregorová, and G. Tichá, "Elasticity of porous ceramicsâĂŤA critical study of modulus- porosity relations," Journal of the European Ceramic Society **26,** 1085–1097 (2006).

[18] K. Phani and S. Niyogi, "Young's modulus of porous brittle solids," Journal of materials science **22,** 257–263 (1987).

[19] J. E. Sader, "Frequency response of cantilever beams immersed in viscous fluids with applications to the atomic force microscope," Journal of applied physics **84,** 64–76 (1998).

[20] S. Basak, A. Raman, and S. V. Garimella, "Hydrodynamic loading of microcantilevers vibrating in viscous fluids," Journal of Applied Physics **99,** 114906 (2006).

Index

Alumina, 8
Aspect Ratio, 5, 10

Cantilever, 1
Chemical Sensor, 1
CNT-M, 5
Cross Section, 13, 14

Density, 12

Ethylene, 8, 9

Fabrication, 7
Flexural Mode, 55
Focused Ion Beam (FIB), 13
Forest, 8
Furnace, 8

Growth, 7

Humidity, 61
Hydrogen, 8, 9

Infiltration, 9
Iron, 8

Laser Deflection, 51
Lock-in Amplifier, 51
Lorentzian Curve, 52

Mass Ratio, 4
Micrometer, 10
Milling, 13

Nanoparticles, 8

Photolithography, 13
Piezoelectric, 49
Pores, 14
Porosity, 13
Porous, 9
Pressure, 63

Resonant Modes, 55

Scanning Electron Microscopy (SEM), 10, 13
Simple Harmonic Oscillator, 52
Solid Cantilever, 3
Synthesis, 8

Torsional Mode, 55